POLITECNICO DI TORINO
Repository ISTITUZIONALE

Enhanced Traction Control on Irregular Roads through Preview-based Nonlinear Model Predictive Control

Original
Enhanced Traction Control on Irregular Roads through Preview-based Nonlinear Model Predictive Control / Manca, R., Stano, P., Mihalkov, M., Castellanos Molina, L.M., Montanaro, U., Tonoli, A., Sorniotti, A.. - In: IEEE ACCESS. - ISSN 2169-3536. - 14:(2026), pp. 94276-94295. [10.1109/access.2026.3696361]

Availability:
This version is available at: 11583/3012700 since: 2026-07-04T09:19:45Z

Publisher:
Institute of Electrical and Electronics Engineers

Published
DOI:10.1109/access.2026.3696361

Terms of use:

This article is made available under terms and conditions as specified in the corresponding bibliographic description in the repository

Publisher copyright

(Article begins on next page)

10 August 2026

IEEE Access
Multidisciplinary | Rapid Review | Open Access Journal

Received 4 May 2026, accepted 18 May 2026, date of publication 25 May 2026, date of current version 25 June 2026.

Digital Object Identifier 10.1109/ACCESS.2026.3696361

RESEARCH ARTICLE

Enhanced Traction Control on Irregular Roads Through Preview-Based Nonlinear Model Predictive Control

RAFFAELE MANCA[1], PIETRO STANO[2], MARIO MIHALKOV[3], LUIS M. CASTELLANOS MOLINA[1], UMBERTO MONTANARO[3], ANDREA TONOLI[1], AND ALDO SORNIOTTI[1], (Member, IEEE)

[1]Department of Mechanical and Aerospace Engineering, Polytechnic University of Turin, 10129 Turin, Italy
[2]Outrigo, 43710 Tarragona, Spain
[3]Department of Mechanical Engineering Sciences, University of Surrey, GU2 7XH Guildford, U.K.

Corresponding author: Aldo Sorniotti (aldo.sorniotti@polito.it)

This work was supported in part by the European Commission through the following projects: EM-TECH (''Innovative e-motor technologies covering e-axles and e-corners vehicle architectures for high-efficient and sustainable e-mobility'') under Grant 101096083; OWHEEL (''Benchmarking of Wheel Corner Concepts Towards Optimal Comfort by Automated Driving'') under Grant 872907; and SmartCorners under Grant 101138110.

ABSTRACT Upcoming V2X technologies and on-board perception systems will provide real-time information from multiple sources, such as other vehicles and the surrounding environment, and thus enable the implementation of innovative active safety control functions. This paper investigates the benefit of the preview on road irregularities on the tire slip control performance of a traction control system for electric vehicles. To this purpose, a nonlinear model predictive controller (NMPC) for traction control is presented, which concurrently uses the information on the tire-road friction factor and upcoming road profile. The simulation results across multiple road scenarios – including comparisons with state-of-the-art benchmarking controllers – highlight the significant improvements brought by the proposed preview-based NMPC, including its robustness with respect to model uncertainties and inaccuracies in the preview information. Preliminary proof-of-concept experiments on an electric vehicle prototype with an on-board powertrain demonstrate the real-time implementability of the algorithm, and confirm the potential of the proposed control solution.

INDEX TERMS Nonlinear model predictive control, active safety systems, road preview, traction control, road irregularities.

LIST OF SYMBOLS

a, b:	Front and rear semi-wheelbases.
a_x, a_y:	Longitudinal and lateral accelerations.
$a_{1,r}$, $b_{1/2,r}$, $c_{1/2,r}$, $d_{1/2,r}$:	Constant coefficients describing the non-linear passive damper characteristics.
A_{car}:	Frontal area of the electric vehicle.
$c_{x,r}$:	Damping coefficient of the suspension bushings.
$c_{r,r}$, $c_{t,r}$:	Radial and tangential damping coefficients of the tire structure.
C_d:	Aerodynamic drag coefficient.
$\hat{e}_\sigma$:	Integral of the longitudinal tire slip violation, averaged over time.
$e_{\sigma_{rj}}$:	Tire slip ratio constraint violation.
f_0, f_2:	Rolling resistance coefficients.
$F_{c,x,rj}$, $F_{k,x,rj}$:	Longitudinal force components through the suspension bushings (damper and spring).
$F_{c,z,rj}$, $F_{k,z,rj}$:	Vertical suspension forces (damper and spring).
F_{drag}:	Aerodynamic drag force.
F_{roll}:	Rolling resistance force.
$F_{r,rj}$, $F_{t,rj}$:	Radial and tangential forces of the tire structure.

The associate editor coordinating the review of this manuscript and approving it for publication was Xiaosong Hu.

© 2026 The Authors. This work is licensed under a Creative Commons Attribution 4.0 License.
For more information, see https://creativecommons.org/licenses/by/4.0/

$F_{x,rj}$: Tire traction/braking force.
$F_{z,ap,rj}$: Longitudinal load transfer contribution through the rigid links of the suspension system.
$F_{z,b,r}$: Rear longitudinal load transfer contribution through the deformable suspension components.
g: Gravitational acceleration.
h_g: Center of gravity height.
H_p: Prediction horizon.
$I_{y,f}$, $I_{y,r}$: Mass moments of inertia of the front or rear rotating parts.
i: Subscript indicating the front or rear axles.
i_t: Gear ratio from the electric motor to the wheel.
$IACA_\delta$: Integral of the absolute value of the steering angle, averaged over time.
j: Subscript indicating the left or right tires.
k: Subscript indicating the position of the previewed value along the prediction horizon.
$k_{x,r}$: Longitudinal stiffness of the suspension bushings.
$k_{r,r}$, $k_{t,r}$: Radial and tangential stiffness of the tire structure.
$k_{z,r}$: Vertical suspension stiffness.
$Lb_{T_{mot}}$, $Ub_{T_{mot}}$: Lower and upper boundaries of the motor torque.
m_{app}: Apparent mass of the vehicle.
m_b: Total sprung mass of the vehicle.
m_{tot}: Total vehicle mass.
$m_{u,f}$, $m_{u,r}$: Individual front and rear unsprung masses.
$M_{y,rj}$: Rolling resistance moment.
M_{rj}: Vector of expected tire-road friction factors.
N_h: Number of steps of the prediction horizon.
p_k: Parameter vector.
$R_{f/r}$: Wheel radius.
$R_{lad,r}$: Laden radius of the rear tires.
s: Traveled distance.
t: Time.
$T_{hs,rj}$: Individual half-shaft torque.
T_{mot}: Actual electromagnetic motor torque.
ΔT_{mot}: Motor torque correction.
$T_{mot,req}$: Requested driver torque.
$T_{mot,req,cr}$: Resulting reference motor torque.
T_c: Normalized computational time.
T_s: Controller sampling time.
u_k: Control input vector.
v_{fin}: Speed at the end of the maneuver.
v_x: Actual longitudinal speed.
$v_{x,ref}$: Reference speed profile.
W_u: Cost function weights.
W_{rj}: Effective road profile height.
x_k: State vector.
$\dot{x}_b$: Longitudinal speed of the sprung mass.
$Z_{rd,rj}$: Road profile ahead along the prediction horizon.
$z_{b,rj}$, $z_{u,rj}$: Vertical displacement of the sprung/unsprung mass.
$z_{rd,rj,k}$: Individual vertical displacement of the road profile.
β_{yj}: Effective road profile slope.
δ: Steering angle.
δ_{sw}: Steering wheel angle.
$\epsilon_{\sigma_{rl/r}}$: Slack variables for slip control.
η_t: Equivalent drivetrain efficiency.
μ: Tire-road friction factor.
$\mu_{rj,k}$: Individual tire-road friction factor.
π_{ref}: Reference curvature.
ρ_{air}: Air density.
ϕ_{rj} : Effective angle formed by the equivalent trailing arm representation of the suspension system.
σ: Longitudinal tire slip.
σ_{peak}: Peak value of the rear longitudinal tire slips.
$\Sigma_{ref,rj}$: Vector of the slip ratio bounds.
$\sigma_{ref,rj,k}$: Slip ratio threshold value.
τ : Motor torque time constant.
$\omega_{rl/r}$: Angular wheel speed.
$\dot{\omega}_{rj}$: Angular wheel acceleration.
$\dot{\psi}$: Yaw rate.

LIST OF ABBREVIATIONS

ABS: Anti-lock braking system.
ACADO: Adopted NMPC development toolkit.
ADAS: Advanced driver assistance systems.
CPU: Central processing unit.
EV: Electric vehicle.
GPS: Global positioning system.
KPI: Key performance indicator.
MPC: Model predictive control.
NMPC: Nonlinear model predictive control or controller.
PID: Proportional integral derivative.
SMC: Sliding mode control.
TCS: Traction control system.
V2I: Vehicle-to-infrastructure.
V2N: Vehicle-to-network.
V2P: Vehicle-to-pedestrian.
V2V: Vehicle-to-vehicle.
V2X: Vehicle-to-everything.
ZEBRA: Zero Emission test bed for Research on Autonomous Driving (the adopted vehicle prototype).

I. INTRODUCTION

Connectivity represents a key aspect of modern intelligent vehicles, which are increasingly characterized by vehicle-to-everything (V2X) communication [1], [2]. V2X technology enables the communication of a considered vehicle – the ego vehicle – with other vehicles (V2V), the infrastructure (V2I), pedestrians (V2P), and the network (V2N), through real-time information exchange [3]. In the context of vehicle safety, V2X has been experimentally evaluated on small vehicle fleets to supply information on the tire-road friction conditions ahead [4], [5].

In parallel, on-board exteroceptive sensors, which provide information on the road and traffic scenario surrounding the ego vehicle, are in use in series production vehicles. For example, the information on the road profile ahead can be acquired through road scanning sensors, such as cameras or lidars, whose outputs can be fused with those from other sensors, through advanced estimation algorithms [6]. Such inputs can be used for ride comfort enhancement through active suspension control [7], [8], [9], see the Magic Body Control system of Mercedes. Conventional model-based tire-road friction estimation methods [10] can also be combined with data from optical sensors and cameras detecting the features of the road ahead [11].

The advent of electric powertrains enables enhanced wheel torque control, due to the generally more accurate and fast torque response compared to internal combustion engines and friction brakes [12]. This can be particularly beneficial for applications such as traction control systems (TCS) [13], anti-jerk controllers [14], stability controllers [15], [16], and ride comfort controllers based on the powertrain torque distribution [17].

The access to data from multiple sources – together with better actuations – can enhance safety and efficiency, and enable collaborative driving and optimized traffic management [18], [19]. Among the available control technologies, model predictive control (MPC) is particularly suitable to incorporate preview information, since it is based on the predictions of the system response, which can be computed from external inputs along a finite horizon [20], [21], [22]. For example, information about the ego vehicle, preceding vehicles, and the surrounding environment can be deployed for adaptive cruise control [23], energy management systems [24], preview-based emergency maneuvering [25], [26], the compensation of the longitudinal vehicle dynamics excited by road irregularities [27], [28], as well as traction control systems (TCS) and anti-lock braking systems (ABS) that benefit from the knowledge of the tire-road friction level ahead [26], [29], [30], [31]. While MPC formulations are naturally suitable to the inclusion of preview information, existing wheel slip control applications primarily exploit friction preview, typically neglecting the effect of the road-profile-induced vertical load variations on the achievable tire-road traction. In parallel to the academic research, the possibility of augmenting vehicle dynamics controllers with preview information on the surrounding environment is also being explored by leading automotive companies. For example, in [32] Ford proposes V2V communication in a vehicle platooning scenario to adjust the operating parameters of the follower vehicles, based on the road surface conditions experienced by the lead vehicle. Similarly, in [33] Hyundai presents a pre-emptive TCS benefitting from the expected tire-road friction conditions. While the available studies focus on the preview of the tire-road friction conditions, the Jaguar Land Rover patents in [34], [35] discuss: i) how the traction levels at the tire-road contact patch are significantly influenced by the wheel-to-surface normal force; and ii) how to use a controllable active suspension system to vary the vertical tire load and enhance the traction capability. However, these approaches focus on managing the vertical load variations induced by the longitudinal and lateral load transfers due to the driving maneuvers, rather than explicitly addressing the impact of road irregularities and their preview on TCS performance. In [36], [37], [38], the effect of road irregularities on the tire-road friction performance has been investigated in braking scenarios. In particular, the effect of undulated surfaces on ABS effectiveness has been analyzed in [36] for ABS on its own. Reference [37] discusses the influence of semi-active suspension settings on ABS performance on rough surfaces, such as Belgian paving and washboard roads, and the study in [38] deals with ABS operation in cooperation with active suspension control, highlighting the challenges posed by the torsional tire dynamics and vertical load variations.

Learning-based wheel slip control approaches have also been investigated in recent years [39], [40]. For example, in [39], neural networks are integrated within an MPC framework to compensate for modeling uncertainties, while reference [40] proposes a fully reinforcement-learning-based traction control strategy. While such methods can capture complex nonlinear tire–road interactions, they typically rely on data-driven controllers with limited interpretability and lack explicit guarantees on constraint satisfaction, stability, and robustness. Moreover, the structured integration of preview information and physical constraints remains challenging, limiting their reliability in safety-critical scenarios.

In summary, while significant progress has been made in preview-based vehicle dynamics control, the literature lacks a systematic investigation of how preview information on road profile and friction conditions can be jointly exploited to enhance TCS performance. To address the identified gap, this study brings the following contributions:

- A novel TCS based on nonlinear model predictive control (NMPC), explicitly integrating preview information on both future tire–road friction levels and road profile-induced vertical load variations within a unified optimal control framework.
- The sensitivity analysis of the performance benefit offered by the proposed control formulation, in comparison with state-of-the-art benchmarking controllers, while considering different dynamic characteristics of

the electric drives, modeling/parametric uncertainties, external disturbances, and inaccuracies in the preview information.

The proposed NMPC is assessed both through simulations and experiments for an electric vehicle (EV) with a centralized on-board powertrain architecture [41], which is the currently dominant layout in the EV market. Nevertheless, because of its flexible prediction model formulation, the algorithm can be easily adapted to different electric powertrain configurations, e.g., based on in-wheel machines. The focus of the manuscript is on the control formulation aspects and potential benefits offered by the preview functionalities. Therefore, the analysis does not encompass the details of the generation of the preview profiles and related sensors, estimators, and connectivity implementations.

The remainder of the paper is organized as follows: Section II introduces the simulation and control system environment, and describes the case study EV; Section III presents the preview-based NMPC TCS formulation; Section IV discusses the considered road scenarios and key performance indicators; Section V analyzes the simulation results; Section VI deals with the proof-of-concept experiments; finally, Section VII summarizes the main conclusions.

II. SIMULATION AND CONTROL ENVIRONMENT AND CASE STUDY VEHICLE

A. SIMULATION AND CONTROL ENVIRONMENT

The simulation and control framework consists of the following functional blocks, shown in Fig. 1:

- The human or automated driver block, which generates the torque request for the rear on-board motor, $T_{mot,req}$, and the steering wheel angle request, $\delta_{sw,req}$. Depending on the maneuver, $T_{mot,req}$ is either imposed in open-loop, or is computed through a proportional integral derivative (PID) cruise controller, which tracks a reference speed profile, $v_{x,ref}\ (t)$, where t is time, and v_x in the figure is the actual longitudinal speed. In the tests with symmetric friction and road irregularity profiles, $\delta_{sw,req}$ is imposed to be zero. In the μ-split (i.e., with asymmetric road conditions on the left and right EV sides) and cornering maneuvers, a trajectory tracking controller generates $\delta_{sw,req}$, based on the combination of feedforward and feedback contributions, where the former uses the kinematic steering condition, and the latter adopts a PID formulation on the curvature error, where the symbol ρ_{ref} in the schematic denotes the reference curvature.
- The V2X block, which outputs the vector M_{rj} of the expected tire-road friction factors along the prediction horizon, i.e., $M_{rj} = \left[\mu_{rj,0}\ \mu_{rj,1}\ \ldots\ \mu_{rj,k}\ \ldots\ \mu_{rj,N_h}\right]$, where $\mu_{rj,k}$ refers to an individual value of the tire-road friction factor; the subscript r indicates that the TCS preview is implemented on the rear axle in the specific application; the subscript j, with $j = l, r$, indicates the left or right tires; and the final subscript k represents the position of the previewed value along the NMPC prediction horizon, with N_h being the number of steps of the prediction horizon.
- The TCS, which represents the novel contribution of the research, and outputs the motor torque correction, ΔT_{mot}, to be applied to the requested driver torque, i.e., the resulting reference motor torque is $T_{mot,req,cr} = T_{mot,req} + \Delta T_{mot}$.
- The nonlinear vehicle model of the case study rear-wheel-drive EV with a single on-board powertrain on the rear axle, linked to the wheels via a single-speed transmission and an open mechanical differential. The plant is implemented in Matlab-Simulink, and considers: i) the electromagnetic torque dynamics of the on-board motor through a transfer function; ii) the axle drivetrain and differential dynamics, with the inclusion of the torsional behavior of the half-shafts; iii) the sprung and unsprung mass dynamics in traction/braking and cornering conditions, described by the longitudinal and lateral force balance equations of the vehicle, the vertical force balance equation of the sprung mass, the roll and pitch moment balance equations of the sprung mass, the yaw moment balance of the vehicle, as well as the longitudinal, vertical and rotational dynamics equations of each unsprung mass, for a total number of 18 degrees of freedom. The model includes the nonlinearities of the suspension dampers, and the longitudinal compliance characteristics related to the suspension bushings. The anti-dive, anti-lift, and anti-squat properties of the suspension system are accounted for in the relevant force and moment balance equations, through an equivalent trailing arm representation of the suspension links; and iv) the tire dynamics through the MF-Swift tire model [42], which is an extensively experimentally validated model for accurate tire-road contact simulation on irregular road surfaces. In the MF-Swift model, the tangential tire forces and moments are calculated by means of the Pacejka magic formula [43], which is enhanced by: a) a three-dimensional enveloping model that employs geometric filtering to capture tire behavior over road irregularities; b) a rigid ring model of the tire structure, accurately simulating tire dynamics up to 100 Hz; and c) residual stiffness and damping models between the contact patch and the rigid ring, to ensure realistic modeling of the total quasi-static tire stiffness in vertical, longitudinal, lateral, and yaw directions.

Although some of the considered simulation conditions involve vehicle cornering, for simplicity and for isolating the effect of the proposed TCS, the preliminary proof-of-concept analysis of this study neglects the presence of the stability control system based on the actuation of the friction brakes.

B. CASE STUDY VEHICLE AND MODEL VALIDATION

The considered EV is the prototype Zero Emission Test Bed for Research on Autonomous Driving (ZEBRA), located at the University of Surrey. ZEBRA is a modified

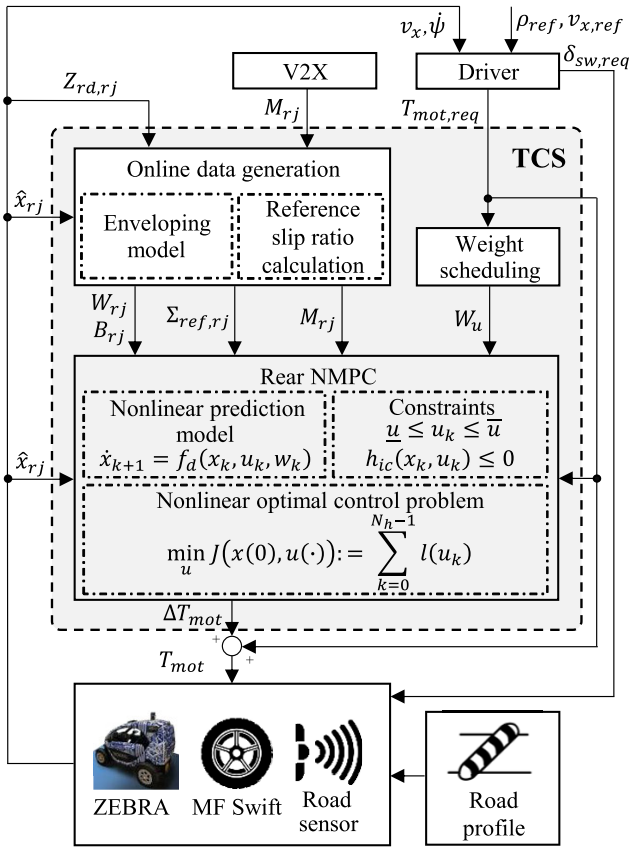

FIGURE 1. Simplified schematic of the simulation and TCS framework.

Renault Twizy, classified as an L7e rear-wheel-drive electric quadricycle, with a centralized on-board electric powertrain, and a drivetrain consisting of a single-speed transmission, open differential, half-shafts, and constant velocity joints. The primary vehicle parameters are in Table 1. The EV is equipped with:

- A set of vehicle dynamics sensors, for measuring the individual wheel speeds, vertical accelerations of the unsprung masses, and vehicle body accelerations in longitudinal, lateral and vertical directions.
- Wire displacement sensors to measure the vertical suspension travel.
- A Racelogic VBOX3i dual GPS (global positioning system) with a fixed base location for precise location information.
- A dSPACE MicroAutoBox II (900 MHz, 16 Mb flash memory) system for the rapid control prototyping of the implemented controllers.

The nonlinear vehicle model in Section II-A, interfaced with the MF-Swift tire model, was experimentally validated along a set of relevant maneuvers, exciting the longitudinal, vertical and lateral dynamics. For example, these included: a) a 4 cm high and 25 cm wide speed bump, followed by a low-friction surface with a friction factor $\mu \approx 0.3$, see Section IV-A for the maneuver description; and b) a skidpad maneuver, in which the experimentally measured steering wheel angle, controlled by a human driver, is directly imposed to the model, while the cruise controller of the simulation architecture tracks the experimental speed profile. The validation results along the two maneuvers are reported in Fig. 2(a) and Fig. 2(b). The good agreement between experiments and simulations makes the high-fidelity model a reliable tool for control system assessment. Moreover, the dynamic performance of the ZEBRA powertrain was validated through tip-in tests, see an example in Fig. 3, which consist of swift torque demand increases to excite the drivetrain dynamics. The validation plot shows the very slow torque response of the powertrain of the specific EV, which can be modeled through a pure time delay of ∼100 ms, in series to a first-order transfer function with a time constant τ of ∼160 ms. Because of the inherently slow response of the specific powertrain, the simulation results in Section V consider a more responsive powertrain as nominal plant, with $\tau = 25$ ms and without pure time delay. This assumption allows illustrating the potential of the proposed TCS when applied to more responsive state-of-the-art powertrain solutions. For completeness, robustness analyses have been included to account for slower torque response characteristics and non-zero pure time delays, see Sections V-C and V-F. Nonetheless, the preliminary experimental results in Section VI confirm the applicability of the proposed algorithm to the slower ZEBRA powertrain, and demonstrate its robustness and effectiveness also in a less than ideal set-up, which is, however, representative of part of the electric powertrain market.

TABLE 1. Main vehicle parameters.

Parameter	Symbol	Value
Vehicle mass	m_{tot}	630 kg
Front semi-wheelbase	a	0.918 m
Rear semi-wheelbase	b	0.768 m
Center of gravity height	h_g	0.46 m
Wheel radius	$R_{f/r}$	0.266 m
Gear ratio from the electric motor to the wheel	i_t	9.23

III. NONLINEAR MODEL PREDICTIVE CONTROLLER FORMULATION

A. CONTROL STRUCTURE

The TCS structure in Fig. 1 is implemented for the rear driving axle, and includes:

- A simplified two-dimensional enveloping model of the two involved tires. The model receives as input the road profile ahead along the prediction horizon, $Z_{rd,rj} = [z_{rd,rj,0}\, z_{rd,rj,1} \ \dots \ z_{rd,rj,k} \ \dots \ z_{rd,rj,\,N_h}]$, where the notation $z_{rd,rj,k}$ denotes the individual vertical displacement. The $z_{rd,rj,k}$ values are generated from a road elevation map, which can be provided by a road scanning sensor. The scanning and information generation methodology of the road profile ahead is beyond the scope of this research. The outputs of the tire

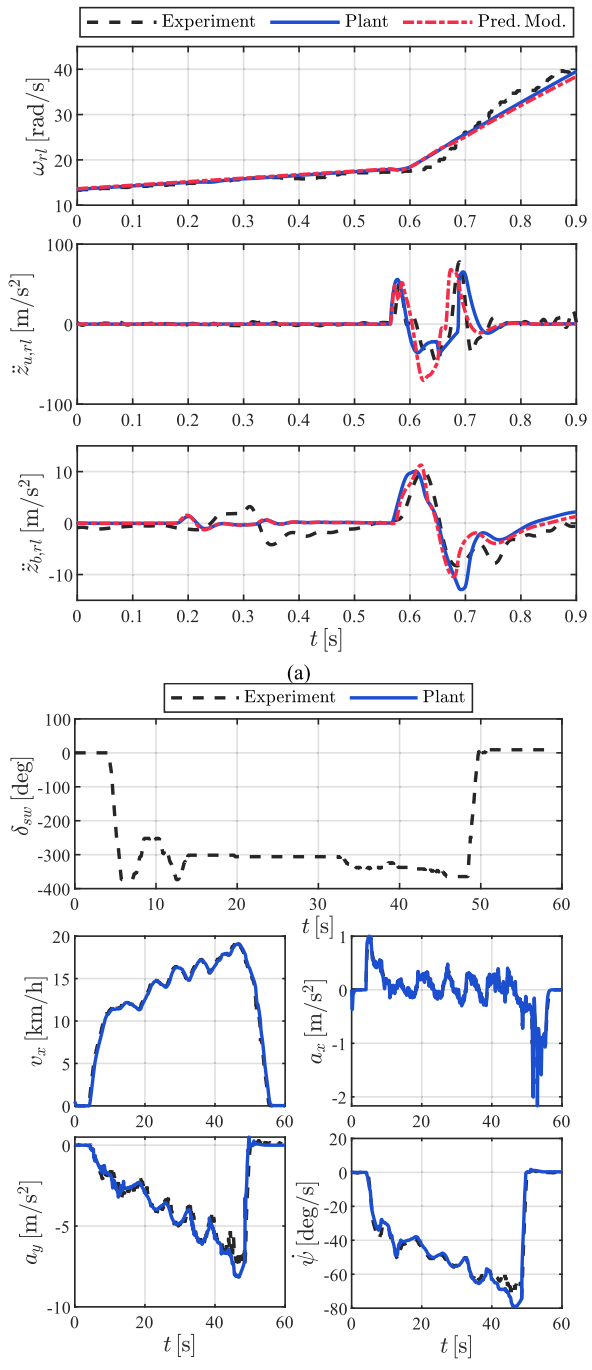

FIGURE 2. Time profiles of: (a) the wheel speed ω_{rl}, vertical unsprung mass acceleration $\ddot{z}_{u,rl}$, and vertical vehicle body acceleration $\ddot{z}_{b,rl}$, for the rear left corner, during the considered speed bump test; and (b) the steering wheel angle δ_{sw}, longitudinal speed v_x, longitudinal and lateral accelerations a_x and a_y, and yaw rate $\dot{\psi}$, during the skidpad maneuver. Comparison of the experimental measurements ('Experiment'), high-fidelity model results ('Plant'), and NMPC prediction model results ('Pred. Mod').

enveloping model are the effective road profile vectors for the height, $W_{rj} = [w_{rj,0}\ w_{rj,1}\ \ldots\ w_{rj,k}\ \ldots\ w_{rj,\,N_h}]$, and slope, $B_{rj} = [\beta_{rj,0}\ \beta_{rj,1}\ \ldots\ \beta_{rj,k}\ \ldots\ \beta_{rj,\,N_h}]$, see Section III-B.

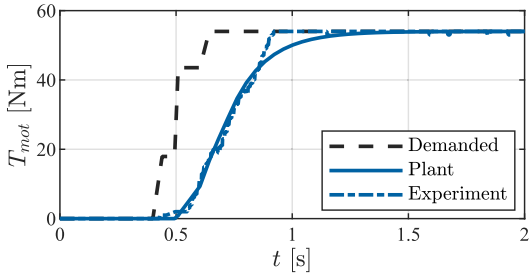

FIGURE 3. Time profiles of the reference motor torque ('Demanded'), torque from the high-fidelity simulation model ('Plant'), and experimentally measured torque ('Experiment', from the inverter current) along a tip-in test.

- The slip ratio threshold generator, which computes the vector of the slip ratio bounds for the rear left and rear right tires, $\Sigma_{ref,rj} = [\sigma_{ref,rj,0}\ \sigma_{ref,rj,1}\ \ldots\ \sigma_{ref,rj,k}\ \ldots\ \sigma_{ref,rj,\,N_h}]$, through two-dimensional look-up tables, as a function of the components μ_{rj} of the expected tire-road friction factor vector, M_{rj}.
- The cost function weight generator, defining the NMPC cost function weights, W_u, which – in the preliminary implementation of this study – are kept constant across the considered maneuvers, but – in a follow-up enhancement – could be scheduled based on the detected road profile ahead.
- The implicit NMPC algorithm for the rear on-board centralized powertrain, which calculates the online solution – in the form of the torque reduction ΔT_{mot} – of the nonlinear optimal control problem, based on a prediction model of the EV rear axle dynamics and the defined set of external inputs.

B. ENVELOPING MODEL

Many significant ride events, affecting both the vertical and longitudinal vehicle dynamics, are caused by road irregularities with similar dimension to the tire-road contact patch. In these circumstances, the enveloping effect of the wheel is not negligible, and thus the raw road profile data obtained from the road scanning sensors cannot be directly used as input into the simplified dynamic tire model embedded in the NMPC algorithms. To this purpose, a tire enveloping model is required to process the road profile measurements, and obtain an effective profile that can be used by the traction controller. To accurately capture the geometric filtering behavior of the tire-road contact patch over an irregular road surface while maintaining computational efficiency, the tandem enveloping model with elliptical cams proposed by Schmeitz [44], [45] is adopted within the proposed control architecture. The model provides a filtered road profile in the form of an effective height w and an effective slope β_y, without requiring numerical integration in the time domain, see [27] for the complete formulation. The two-cam algorithm is calibrated based on the more complex MF-Swift model integrated into

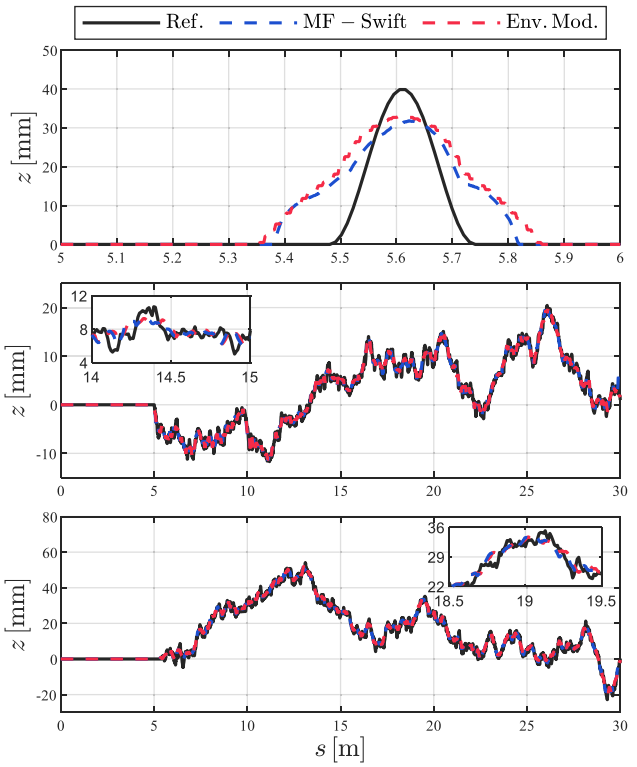

FIGURE 4. Comparison of the effective road profiles generated by the MF-Swift tire model ('MF-Swift') and the tandem enveloping model ('Env. Mod.'), starting from raw road profile data ('Ref') in terms of vertical displacement, along (from top to bottom) a 4 cm high and 25 cm wide speed bump, an ISO class B road profile, and an ISO class C road profile, where s is the traveled distance.

the high-fidelity nonlinear vehicle model for control system assessment.

To validate the geometric filter, Fig. 4 compares typical road elevation profiles, which would be the output of a road scanning sensor (labelled as 'Ref', which is the main input toward the enveloping models), with the corresponding effective profiles generated by the MF-Swift model ('MF-Swift') and the two-cam enveloping model ('Env. Mod.'), for the road scenarios described in Section IV-A, corresponding to a speed bump, and sections of ISO class B and class C roads. The results show: i) a close agreement between the two-cam and MF-Swift models, which confirms the reliability of the simplified model for control purposes; and ii) a significant wheel enveloping effect for road irregularities with comparable dimensions to the tire-road contact patch, see the difference between 'Ref.' and the model outputs in the first scenario. As a result, in these conditions the raw road profile data from scanning sensors cannot be directly used for accurate prediction within the NMPC algorithms.

C. PREDICTION MODEL

Differently from linear model predictive control, NMPC enables to use nonlinear model formulations to predict and optimize the system dynamics. The decision to select NMPC is driven by the inherent nonlinearities that dominate the vehicle dynamics when traversing road irregularities (e.g., speed bumps, potholes) at the limits of adhesion, specifically: i) the shock absorber characteristics; ii) the trigonometric functions to resolve the radial and tangential tire forces when the road slope changes abruptly; and iii) the tangential tire force dependencies on the longitudinal slip and vertical tire load.

The formulation of the prediction model, i.e., the model implemented within the NMPC algorithm to generate the associated prediction, is inspired by those of recent controllers targeting EV comfort enhancement [27], [28], and includes: a) the tire and wheel dynamics of each rear corner; b) the vertical and longitudinal unsprung mass dynamics of the same corners; c) the vertical dynamics of the rear sprung mass; and d) the longitudinal dynamics of the sprung mass of the entire vehicle. Since the focus is on the rear driving axle, the model neglects the vertical and longitudinal dynamics of the front unsprung masses. As a result, from a mechanical perspective, the system is characterized by eight degrees of freedom. Additionally, a differential equation describes the torque dynamics of the rear electric drive, whose torque is evenly distributed between the left and right wheels.

Due to the substantial symmetry of the vehicle, Fig. 5 shows only the left side view of the prediction model. m_{app} represents the apparent mass of the vehicle, which includes the effects of the relevant rotating parts. Since the model focuses on the rear axle dynamics, the inertia of the rotating components of the rear axle, e.g., the wheels and motor rotor, is directly considered in the rear wheel torque balance equations. On the contrary, m_{app} includes the mass moment of inertia of the front wheels, which contribute to the overall vehicle inertia, but are not detailed in the prediction model. Such simplification – together with neglecting the torsional and backlash dynamics of the rear drivetrain, which are not very significant in the specific EV – allows for a computationally efficient prediction that captures the essential dynamics while accounting for the correct overall inertia. The unsprung mass includes a central non-rotating body, corresponding to the suspension upright, part of the suspension arms, and the brake caliper, and an outer rotating part, accounting for the wheel rim and brake disc. The suspension spring and shock absorber are modeled through vertical stiffness and nonlinear damping elements between the sprung and unsprung masses. The compliance effect of the suspension bushings of each rear corner are replicated through longitudinal springs and a dampers, with stiffness $k_{x,r}$ and damping coefficient $c_{x,r}$.The road irregularities affect both the vertical and longitudinal dynamics of the sprung mass. The dynamics of the tire structure are modeled through two couples of spring-damper systems, the first one radial, with stiffness $k_{r,r}$ and damping coefficient $c_{r,r}$, and a second one tangential, with stiffness $k_{t,r}$ and damping coefficient $c_{t,r}$. These elements of the tire structure transmit their forces directly to the non-rotating part of the unsprung mass, and are assumed to be in contact with the road through a frictionless roller system. The

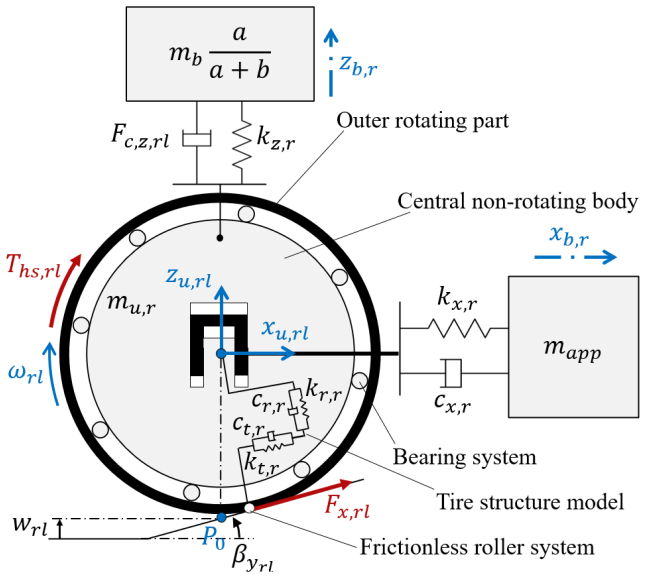

FIGURE 5. Lateral view of the left side of the NMPC prediction model.

longitudinal tire force resulting from the longitudinal tire slip is independently applied to the rotating part of the unsprung mass, and then transmitted to its non-rotating part through the bearing system in Fig. 5. The proposed setup offers sufficient accuracy while greatly simplifying the formulations with respect to (w.r.t.) the MF-Swift tire model. The model is easily adaptable to other EV architectures with centralized on-board motor/s, e.g., front-wheel-drive and rear-wheel-drive EVs, where – based on requirements – it can be augmented with the torsional drivetrain dynamics, as well as to different powertrain solutions, e.g., with direct drive in-wheel machines.

The prediction model dynamics of the considered rear-wheel-drive EV are described by the following equations:

- Electromagnetic torque dynamics of the centralized rear motor

$$\dot{T}_{mot} = \left[T_{mot,req,cr} - T_{mot}\right] \frac{1}{\tau} \tag{1}$$

where T_{mot} is the actual electromagnetic motor torque; and τ is the respective time constant.

- Vertical force balance of the rear sprung mass

$$\ddot{z}_{b,r} = \left\{ \sum_{j=l,r} \left[-F_{k,z,rj} - F_{c,z,rj}\right] + F_{z,b,r} \right\} \frac{1}{m_b} \frac{a+b}{a} \tag{2}$$

where m_b is the total sprung mass of the vehicle; $F_{k,z,rj}$ and $F_{c,z,rj}$ are the vertical suspension forces, associated with the spring and shock absorber of each rear corner; and $F_{z,b,r}$ is the rear longitudinal load transfer contribution going through the deformable suspension components, i.e., the springs and shock absorbers. More specifically, $F_{k,z,rj}$ is given by:

$$F_{k,z,rj} = k_{z,r} \left[z_{b,rj} - z_{u,rj}\right] \tag{3}$$

where $k_{z,r}$ is the vertical suspension stiffness; and $z_{u,rj}$ is the vertical displacement of the unsprung mass of the considered rear corner. $F_{c,z,rj}$ is calculated with a continuous nonlinear function that approximates the passive damper behavior:

$$F_{c,z,rj} = a_{1,r} + b_{1,r} \text{atan}\left(c_{1,r}\left[\dot{z}_{b,rj} - \dot{z}_{u,rj}\right] + d_{1,r}\right) + b_{2,r} \text{atan}\left(c_{2,r}\left[\dot{z}_{b,rj} - \dot{z}_{u,rj}\right] + d_{2,r}\right) \tag{4}$$

where $a_{1,r}$, $b_{1/2,r}$, $c_{1/2,r}$, and $d_{1/2,r}$ are constant coefficients. $F_{z,b,r}$ is given by:

$$F_{z,b,r} = m_{tot}\ddot{x}_b \frac{h_g}{a+b} - \sum_{j=l,r} F_{z,ap,rj} \tag{5}$$

where h_g is the center of gravity height; m_{tot} is the total vehicle mass; and $F_{z,ap,rj}$ is the longitudinal load transfer contribution that is transmitted through the rigid links of the suspension system, because of the suspension anti-properties (e.g., anti-dive, anti-lift, and anti-squat):

$$F_{z,ap,rj} = \frac{1}{2} m_{tot}\ddot{x}_b \tan\phi_{rj} \tag{6}$$

where ϕ_{rj} is the effective angle formed by the equivalent trailing arm representation of the specific suspension system.

- Vertical force balance of the unsprung mass of each rear corner

$$\ddot{z}_{u,rj} = \left[F_{c,z,rj} + F_{k,z,rj} + F_{r,z,rj} - F_{t,z,rj} + F_{x,z,rj} - F_{z,ap,rj}\right] \frac{1}{m_{u,r}} \tag{7}$$

where $m_{u,r}$ is the relevant unsprung mass; and $F_{r,z,rj}$ and $F_{t,z,rj}$ are the vertical components of the radial and tangential forces, $F_{r,rj}$ and $F_{t,rj}$, related to the tire structure, which are given by:

$$F_{r,rj} = k_{r,r}\left[w_{rj} - z_{u,rj}\right]\cos\beta_{y,rj} + c_{r,r}\left[\dot{w}_{rj} - \dot{z}_{u,rj}\right]\cos\beta_{y,rj} \tag{8}$$

$$F_{t,rj} = k_{t,r}\left[w_{rj} - z_{u,rj}\right]\sin\beta_{y,rj} + c_{t,r}\left[\dot{w}_{rj} - \dot{z}_{u,rj}\right]\sin\beta_{y,rj} \tag{9}$$

under the assumption of neglecting the time derivative of $\beta_{y,rj}$. $F_{x,z,rj}$ is the vertical component of the traction/braking force of the tire, $F_{x,rj}$, obtained with version 5.2 of the Pacejka model [43] for zero slip angle conditions.

- Longitudinal force balance of the EV sprung mass

$$\ddot{x}_b = \left\{ \sum_{j=l,r} \left[-F_{k,x,rj} - F_{c,x,rj}\right] - F_{drag} - F_{roll,f} \right\} \frac{1}{m_{app}} \tag{10}$$

where the traction force is transmitted to the sprung mass through the suspension bushings, whose longitudinal force components are $F_{k,x,rj}$ and $F_{c,x,rj}$:

$$F_{k,x,rj} = k_{x,r}\left[x_{b,rj} - x_{u,rj}\right] \tag{11}$$
$$F_{c,x,rj} = c_{x,r}\left[\dot{x}_{b,rj} - \dot{x}_{u,rj}\right] \tag{12}$$

In (10), the aerodynamic drag force, F_{drag}, is calculated as:

$$F_{drag} = \frac{1}{2}\rho_{air} C_d A_{car} \dot{x}_b^2 \tag{13}$$

where ρ_{air} is the air density; C_d is the aerodynamic drag coefficient; and A_{car} is the frontal area of the EV. The rolling resistance force of the front axle, $F_{roll,f}$, is expressed as:

$$F_{roll,f} = f_{roll,f} m_{tot} \frac{b}{a+b} g \tag{14}$$

where $f_{roll,f}$ is the rolling resistance coefficient, given by:

$$f_{roll} = f_0 + f_2 \dot{x}_b^2 \tag{15}$$

with f_0 and f_2 being constant coefficients. The apparent mass m_{app} is defined as:

$$m_{app} = m_b + 2m_{u,f} + \frac{2I_{y,f}}{R_f^2} \tag{16}$$

where $m_{u,f}$ is the individual front unsprung mass; $I_{y,f}$ includes the mass moments of inertia of the rotating parts of the front corners; and R_f is the rolling radius of the front tires.

- Longitudinal force balance of the individual rear unsprung mass

$$\ddot{x}_{u,rj} = \left[F_{c,x,rj} + F_{k,x,rj} - F_{r,x,rj} - F_{t,x,rj} + F_{x,x,rj}\right] \frac{1}{m_{u,r}} \tag{17}$$

where $F_{r,x,rj}$, $F_{t,x,rj}$, and $F_{x,x,rj}$ are the longitudinal components of $F_{r,rj}$, $F_{t,rj}$, and $F_{x,rj}$.

- Individual rear wheel moment balance

$$\dot{\omega}_{rj} = \left[T_{hs,rj} - F_{x,rj} R_{lad,r} - M_{y,rj}\right] \frac{1}{I_{y,r}} \tag{18}$$

where $\dot{\omega}_{rj}$ is the angular wheel acceleration; $M_{y,rj}$ is the rolling resistance moment of the specific tire and drivetrain; $R_{lad,r}$ is the laden radius of the rear tires; and $T_{hs,rj}$ is the individual half-shaft torque:

$$T_{hs,rj} = \frac{1}{2} i_t \eta_t T_{mot} \tag{19}$$

where i_t and η_t are the gear ratio and equivalent drivetrain efficiency.

The NMPC prediction model, described by (1)-(19), is rearranged in a discrete nonlinear state-space form:

$$x_{k+1} = f_d\left(x_k, u_k, p_k\right) \tag{20}$$

where f_d indicates the corresponding discrete nonlinear function; and x_k, u_k, and p_k are the state, control input, and parameter vectors, with the subscript k indicating a generic time step along the prediction horizon. x_k is defined as:

$$x_k = \left[\dot{z}_{b,r}\ z_{b,r}\ \dot{z}_{b,rl} - \dot{z}_{u,rl}\ z_{b,rl} - z_{u,rl}\ \dot{z}_{b,rr} - \dot{z}_{u,rr}\ z_{b,rr} - z_{u,rr}\ \dot{x}_b\ x_b\ \dot{x}_{u,rl}\ x_{u,rl}\ \dot{x}_{u,rr}\ x_{u,rr}\ \omega_{rl}\ \omega_{rr}\ T_{mot}\right]^T \tag{21}$$

where, for simplicity, here and in the remainder the subscript k is omitted from the symbols of the individual components of the vectors. u_k is given by:

$$u_k = \left[\Delta T_{mot}\ \ \varepsilon_{\sigma_{rl}}\ \ \varepsilon_{\sigma_{rr}}\right]^T \tag{22}$$

where the actual control input applied to the plant, ΔT_{mot}, is complemented by the virtual control inputs represented by the slack variables, $\varepsilon_{\sigma_{rl/r}}$, which are used to impose the soft constraints on the longitudinal tire slip, see Section III-D. p_k includes the expected effective road profile, the tire-road friction factor information, the slip ratio threshold value, and the torque demand before the TCS correction:

$$p_k = \left[w_{rl}\ \ \beta_{y,rl}\ \ w_{rr}\ \ \beta_{y,rr}\ \ \mu_{rl}\ \ \sigma_{ref,rl}\ \ \mu_{rr}\ \ \sigma_{ref,rr}\ \ T_{mot,req}\right]^T \tag{23}$$

where – in the NMPC implementations with road preview – w_{rj}, $\beta_{y,rj}$, μ_{rj}, and $\sigma_{ref,rj}$ vary along the prediction horizon $H_p = \sum_{k=0}^{N_h-1} T_{s,k}$, with $T_{s,k}$ being the controller sampling time at the considered prediction step, and N_h the number of prediction steps. The preview parameters at the step k are computed based on the expected traveled distance of the wheel over N_h, which is calculated as $x_{u,rj,k} = x_{u,rj,0} + \dot{x}_{u,rj,0} \sum_{n=0}^{k} T_{s,n}$, with $\dot{x}_{u,0}$ being the longitudinal unsprung mass speed at the current time step, and the subscript n indicating the relevant prediction steps. The assumption of constant speed throughout the prediction horizon is reasonable for the considered short H_p values.

Despite being based on a completely independent and significantly more basic formulation w.r.t. the simulation model for control system assessment, Fig. 2(a) confirms the good alignment of the prediction model with the experimental data.

D. NONLINEAR OPTIMAL CONTROL PROBLEM

At each time step, the nonlinear optimal control problem formulation aims to minimize the cost function J, according to:

$$\begin{aligned} \min_u J\left(x\left(0\right), u\left(\cdot\right)\right) &:= \sum_{k=0}^{N_h-1} l\left(u_k\right) \\ \text{s.t.}\quad & x_0 = x_{in} \\ & x_{k+1} = f_d\left(x_k, u_k, p_k\right) \\ & \underline{u} \le u_k \le \overline{u} \\ & h_{ic}\left(x_k, u_k\right) \le 0 \\ & u\left(\cdot\right) : [0, N_h - 1] \end{aligned} \tag{24}$$

where $u(\cdot) = \left[u_0\, u_1 \ldots\ldots u_{N_h}\right]^T$ is the sequence of augmented control input vectors along H_p, which in this case coincides with the control horizon; x_{in} is the initial value of the state vector; $\underline{u}$ and $\overline{u}$ are vectors including the lower and upper bounds of the control input u; h_{ic} is the inequality constraint function; and $l(u_k)$ is the stage cost, which is given by:

$$l(u_k) = W_{u,\Delta T_{mot}} \Delta T_{mot,k} + \sum_{j=l,r} W_{u,\varepsilon_{\sigma r}} \varepsilon_{\sigma_{rj},k} \tag{25}$$

where $W_{u,\Delta T_{mot}}$ and $W_{u,\varepsilon_{\sigma_r}}$ are weights, respectively penalizing the TCS-induced torque reduction and the slack variables.

The control input and inequality constraints are:

$$Lb_{T_{mot}} \leq T_{mot,req} + \Delta T_{mot,k} \leq Ub_{T_{mot}} \tag{26}$$

$$\sigma_{rj,k} \leq \sigma_{ref,rj,k} + \varepsilon_{\sigma_{rj,k}} \tag{27}$$

$$\varepsilon_{\sigma_{rj,k}} \geq 0 \tag{28}$$

where $Lb_{T_{mot}}$ and $Ub_{T_{mot}}$ are the lower and upper boundaries of the motor torque, implemented as hard constraints; and (27) and (28) are soft constraints on the violation of the longitudinal slip ratio threshold, $\sigma_{ref,rj,k}$, generated from predetermined lookup tables, see Section III-A, to keep – during traction control events – the longitudinal tire slip ratio $\sigma_{rj,k}$ close to the value corresponding to the maximum traction force for each friction factor $\mu_{rj,k}$. $\sigma_{rj,k}$ is expressed as:

$$\sigma_{rj,k} = 1 - \frac{\dot{x}_{u,rj,k}}{\omega_{rj,k} R_r} \tag{29}$$

The proposed NMPC prediction model explicitly captures the road-induced variations of the vertical tire loads, which affect the predicted longitudinal slip and longitudinal force profiles. This represents a key difference from the available traction control approaches based on simplified models that neglect the vertical load dynamics. Although vertical dynamics terms are not explicitly included in the implemented cost function formulation, the framework readily allows their addition (e.g., for achieving a ride comfort enhancement), which will be addressed in future work.

E. CONTROLLER IMPLEMENTATION

The ACADO toolkit, which offers a robust platform for NMPC development [46], is employed to implement the controllers. The selected solver settings include the qpOASES optimization algorithm, the fourth-order Runge-Kutta integrator, and the multiple shooting discretization method. In the proposed formulation, the calibration of the cost function weights is straightforward, since the main control objective is enforced through a soft constraint on the tire slip ratio via a slack variable, rather than through continuous tracking of a reference profile. Consequently, a brute-force search was adopted to determine constant values of the weights valid across all simulated maneuvers, controller variants, and parameter settings (e.g., in terms of H_p and $T_{s,k}$), as detailed in the following sections.

IV. PERFORMANCE ASSESSMENT

A. CONSIDERED ROAD PROFILES

The controller performance is evaluated along:

1) A speed bump test, consisting of a 4 cm high and 25 cm wide speed bump, followed by low-friction patch with a tire-road friction factor $\mu \approx 0.3$. This set-up is also replicated in the experimental tests.
2) Irregular road profile tests, corresponding to the sections in Fig. 4 of standardized ISO class B and class C roads [47], [48], with variable tire-road friction levels, i.e., with a first μ-jump from 1 to 0.4, a second one from 0.4 to 1, and a third one from 1 to 0.3.
3) A straight-line speed bump test in μ-split conditions from 30 km/h, consisting of the same road profile as in 1), followed by a low-friction patch only for the left wheels, with a tire-road friction factor $\mu \approx 0.3$. The approximately straight-line trajectory of the vehicle is maintained through the feedforward and feedback steering controller for path tracking.
4) A speed bump test in μ-split conditions during right-hand cornering from 10 km/h, with linearly increasing reference curvature from 0 to 0.17 m^{-1} in 3 s, also in this case tracked through the path following controller.

In 1)-4), the torque demand is kept at the maximum level (57 Nm) that is allowed by the ZEBRA powertrain.

B. KEY PERFORMANCE INDICATORS

The following set of key performance indicators (KPIs) is used to evaluate the TCS performance:

- The peak value, σ_{peak}, of the rear longitudinal tire slips, along the considered test:

$$\sigma_{peak} = \max\left(\max_t(\sigma_{rl}), \max_t(\sigma_{rr})\right) \tag{30}$$

  where the notation $\max_t(\,)$ indicates the maximum value along a time series of data.
- The integral of the longitudinal tire slip violation, $\hat{e}_\sigma$, averaged over time:

$$\hat{e}_\sigma = \frac{1}{t_{fin} - t_{in}} \int_{t_{in}}^{t_{fin}} \left[e_{\sigma_{rl}} + e_{\sigma_{rr}}\right] dt \tag{31}$$

  where t_{in} and t_{fin} are the initial and final times of the relevant part of the test, e.g., the one in which the rear wheels are on the low-friction surface in the speed bump test, and the whole road section with geometric irregularities in the ISO road profile tests; and $e_{\sigma_{rl}}$ and $e_{\sigma_{rr}}$ are the tire slip constraint violations, which define the extent by which the actual tire slip exceeds the threshold value in traction conditions:

$$e_{\sigma_{rj}} = \text{sat}\left(\sigma_{rj} - \sigma_{ref,rj}\right)_0^\infty \tag{32}$$

- The speed at the end of the maneuver, v_{fin}, which is an indicator of the resulting longitudinal acceleration performance.

For the maneuvers involving μ-split conditions, also the following indicators are considered, to assess the level of

excitation of the lateral vehicle dynamics induced by the tire-road friction asymmetry:

- The maximum absolute value of the lateral acceleration $|a_y|_{max}$, computed in the relevant part of the test, i.e., during the μ-split-provoked transient.
- The integral of the absolute value of the steering angle averaged over time:

$$IACA_\delta = \frac{1}{t_{fin} - t_{in}} \int_{t_{in}}^{t_{fin}} |\delta| \, dt \tag{33}$$

V. SIMULATION RESULTS

The simulations of this section are based on the experimentally validated nonlinear vehicle model described in Section II. The performance of the proposed NMPC configuration, referred to as NMPC$^{(\text{full prev})}$, benefitting from the pre-emptive information on both the road profile and friction factor ahead, is compared with the one of: i) NMPC$^{(\mu \text{ prev})}$, which, w.r.t. NMPC$^{(\text{full prev})}$, excludes the pre-emptive information on the road profile ahead; ii) NMPC$^{(\text{w/o prev})}$, which does not consider any preview information; iii) a TCS based on the integral sliding mode control (SMC) formulation in [49] and [50], which is adapted to traction conditions (the original implementation is for braking), and is sampled at 1 ms unless otherwise specified; and iv) the passive vehicle, i.e., without TCS.

A. SENSITIVITY ANALYSIS ON SAMPLING TIME AND PREDICTION HORIZON

The target is to identify the optimal control settings for NMPC$^{(\text{full prev})}$, i.e., the controller sampling time T_s – in this case maintained constant during the prediction – and prediction horizon H_p, along the speed bump test. The discretization time T_d, i.e., the integration time step of the prediction model, is set to 1 ms throughout the following analyses, which provides adequate prediction stability and accuracy. A single tuning of the cost function weights is used, providing desirable performance across the NMPC configurations as well as all the considered T_s and H_p values. Fig. 6 reports the nondimensional computational time $\bar{T}_c$, representing the normalized average central processing unit (CPU) time along the selected maneuver, as a function of σ_{peak} and $\hat{e}_\sigma$, which was computed on a personal computer with an Intel Corei7 1185G7 CPU (3.0 GHz, 4 core, 8 threads). The normalization – which makes the result independent from the specific computing hardware – is relative to the minimum value of the average computational time among the considered control settings, which is achieved by the configuration with $T_s = 10$ ms and $H_p = 30$ ms. For given H_p, small sampling times, e.g., $T_s = 1$ ms, lead to excessive computational loads. In this respect, $\bar{T}_c$ exhibits a nonlinear relationship as a function of T_s, with an evident decrease when transitioning from $T_s = 1$ ms to $T_s = 5$ ms, and a more moderate reduction from $T_s = 5$ ms to $T_s = 10$ ms. In parallel, short prediction horizons, e.g., H_p =30 ms, bring sub-optimal TCS performance in

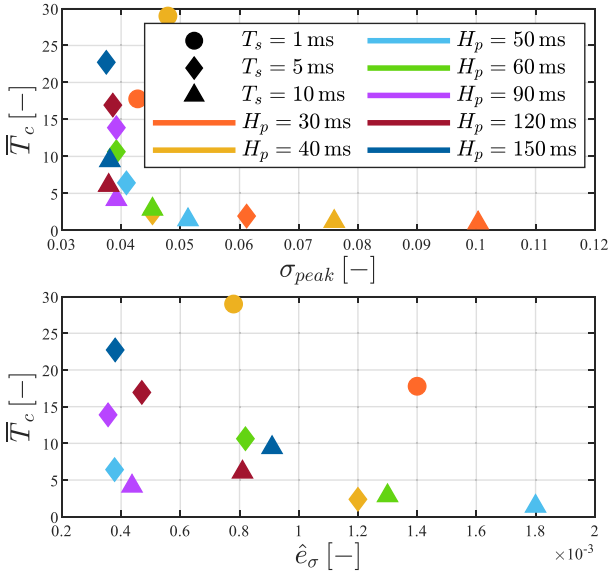

FIGURE 6. $\bar{T}_c$ as a function of σ_{peak} and $\hat{e}_\sigma$, for different values of T_s and H_p, for NMPC$^{(\text{full prev})}$.

terms of longitudinal slip limitation. In fact, in contrast with conventional purely feedback-based TCSs, NMPC$^{(\text{full prev})}$ requires longer horizons to account and compensate for the effect of the previewed road irregularities and the related predicted vertical tire force variations on the longitudinal slip response. Such need can be attributed to the pre-emptive nature of the torque modulation, which is able to effectively address the slip ratio dynamics, also in presence of the response delays caused by the motor torque time constant and controller sampling time, provided the algorithm is given a sufficiently long time, i.e., H_p, to plan the appropriate reference torque correction profile. In fact, the control input is delayed and filtered by the vehicle plant before reaching the wheel. Hence, as H_p increases, σ_{peak} tends to decrease, until it saturates at ∼0.038, which is close to the wheel slip threshold in the low-friction patch. However, longer horizons than 90 ms do not bring any further benefit, and can result in marginally worse performance, e.g., see $\hat{e}_\sigma$ for $H_p = 120$ ms, in addition to increased computational cost. Also, the KPI variation caused by T_s tends to decrease while increasing H_p, e.g., compare the KPIs for $H_p = 50$ ms and 90 ms.

The important conclusion is that, for the simulated EV with a powertrain time constant $\tau = 25$ ms, the controller configuration with $T_s = 10$ ms and $H_p = 90$ ms strikes a desirable trade-off between the longitudinal slip control performance, expressed by σ_{peak} and $\hat{e}_\sigma$, and the computational effort, expressed by $\bar{T}_c$. The result would be different in case of a slower powertrain response, which would require a larger H_p to achieve the best performance, see Section V-C.

B. SPEED BUMP TEST RESULTS

For the speed bump test, Fig. 7 reports the profiles of the main variables as a function of the traveled distance, s, for the

passive EV, as well as for the same EV with NMPC$^{(\text{full prev})}$, NMPC$^{(\mu\ \text{prev})}$, NMPC$^{(\text{w/o prev})}$, and SMC. The response of each NMPC configuration is included for: a) T_s =10 ms and H_p = 90 ms, i.e., the best NMPC$^{(\text{full prev})}$ setting, based on the results in Section V-A; and b) T_s = 5 ms and H_p = 50 ms, which is a sub-optimal setting in terms of NMPC$^{(\text{full prev})}$ performance, since the short prediction horizon does not enable effective preview-based slip compensation with the considered powertrain torque dynamics. However, because of the lower implementation time and the fact that a relatively long H_p is not especially useful in case of absence of preview, setting b) could be more suitable than a) to the other controller configurations, see the sensitivity results in [51]. The cost function weights are kept constant across the analysis, and equal to values – different from those in Section V-A – that are especially suitable for the two considered prediction horizons, which results in marginally better KPI values.

Given the symmetry of the selected road profile, the figure plots the slip ratio only for the rear left corner. The combined preview information of NMPC$^{(\text{full prev})}$ enables nearly full compensation of the slip constraint violation, with σ_{peak} values of 0.032 and 0.041 for settings a) and b), thanks to the pre-emptive modulation of the rear motor torque. Despite the pre-emptive powertrain torque reduction, *NMPC*$^{(\text{full prev})}$ achieves higher final EV speed than the passive case, and negligible speed profile difference w.r.t. NMPC$^{(\mu\ \text{prev})}$, NMPC$^{(\text{w/o prev})}$, and SMC. On the contrary, due to the partial or complete lack of knowledge of the friction and road profiles ahead, NMPC$^{(\mu\ \text{prev})}$, NMPC$^{(\text{w/o prev})}$, and SMC struggle effectively compensating the slip threshold violation. For example, σ_{peak} reaches 0.11 and 0.17 for setting a), and 0.08 and 0.13 for b), respectively with NMPC$^{(\mu\ \text{prev})}$ and NMPC$^{(\text{w/o prev})}$, which confirms that, in absence of complete road preview, T_s is more impactful than H_p for predictive control design. SMC slightly outperforms NMPC$^{(\text{w/o prev})}$ in terms of slip ratio limitation and tracking, while remaining far from NMPC$^{(\text{full prev})}$. However, the sliding mode algorithm exhibits a torque chattering effect at a frequency of ∼15 Hz, which can cause passenger discomfort because of the transmission of the localized vibrations through the vehicle structure [52].

C. SENSITIVITY TO THE ACTUATION DYNAMICS

The objective is to evaluate the impact of different torque time constants of the powertrain, i.e., τ = 60, 90, and 120 ms, on the TCS performance during the simulated speed bump test. The assessment is conducted for two control settings, with H_p = 90 and 150 ms, both of them characterized by T_s = 10 ms.

As expected, the σ_{peak} and $\hat{e}_\sigma$ histograms in Fig. 8 highlight a generalized performance decay as τ increases. Consistently with Section V-B, the NMPC$^{(\text{full prev})}$ implementations with H_p = 150 ms provide better response than those operating at H_p = 90 ms, while the opposite trend occurs for NMPC$^{(\text{w/o prev})}$ and NMPC$^{(\mu\ \text{prev})}$. For τ = 60 ms,

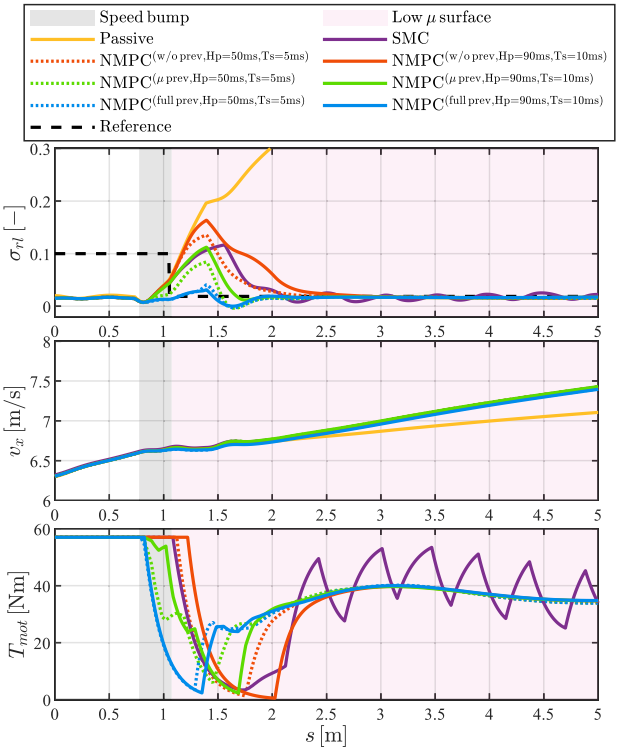

FIGURE 7. Performance comparison in terms of σ_{rl}, v_x, and T_{mot} profiles as a function of s, during the considered speed bump test, simulated with the passive EV, and the same EV with SMC, and two settings, i.e., T_s = 10 ms and H_p = 90 ms (continuous lines), and T_s = 5 ms and H_p = 50 ms (dashed line), of NMPC$^{(\text{full prev})}$, NMPC$^{(\mu\ \text{prev})}$, and NMPC$^{(\text{w/o prev})}$. Here and in the remainder, the grey areas highlight the speed bump location; the pink regions indicate the low-friction surfaces; and the dashed line refers to the longitudinal slip threshold profile.

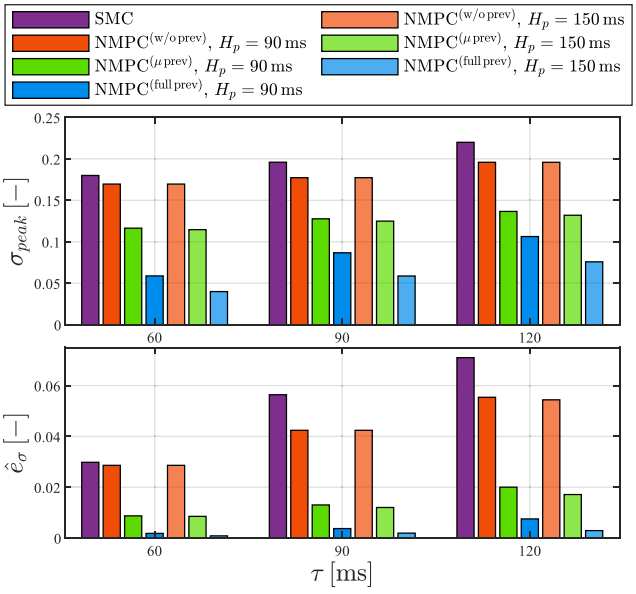

FIGURE 8. σ_{peak} and $\hat{e}_\sigma$ for the rear left corner, for different values of τ and H_p, for the NMPC configurations and SMC along the considered speed bump test.

NMPC$^{(\text{full prev})}$ with H_p = 90 ms reduces σ_{peak} and $\hat{e}_\sigma$ by 65% and 94% w.r.t. the corresponding NMPC$^{(\text{w/o prev})}$

setting, and by 50% and 79% w.r.t. NMPC$^{(\mu\ \text{prev})}$. For $H_p = 150$ ms, the σ_{peak} and $\hat{e}_\sigma$ reductions amount to 76% and 97% w.r.t. NMPC$^{(\text{w/o prev})}$, and to 65% and 95% w.r.t. NMPC$^{(\mu\ \text{prev})}$. Intuitively, the benefit of a longer prediction horizon is more evident for the slowest EM dynamics, i.e., for $\tau = 120$ ms, with NMPC$^{(\text{full prev})}$ operating with $H_p = 150$ ms reducing σ_{peak} and $\hat{e}_\sigma$ by 61% and 95% w.r.t. NMPC$^{(\text{w/o prev})}$, and 42% and 83% w.r.t. NMPC$^{(\mu\ \text{prev})}$. This represents a further decrease of $\hat{e}_\sigma$ by 8% and 21% for NMPC$^{(\text{full prev})}$ w.r.t. NMPC$^{(\text{w/o prev})}$ and NMPC$^{(\mu\ \text{prev})}$, in comparison with the setting with $H_p = 90$ ms. Interestingly, SMC is more affected by the powertrain dynamics than NMPC$^{(\text{w\o prev})}$, see the increment of the gap between the respective KPI bars as τ increases, which highlights the benefit of predictive algorithms in case of systems with slow actuation dynamics. Although the considered EM actuations are purposely slower than the best industrially available solutions, the important conclusion is that NMPC$^{(\text{full prev})}$ consistently delivers excellent performance across varying actuation time constants, making it a viable choice for application across the diverse implementations of the current electric powertrain market.

D. CONTROLLER EVALUATION FOR DIFFERENT SYMMETRIC ROAD AND FRICTION PROFILES

The profiles of the main variables for the two sections of the ISO class B and ISO class C roads in Fig. 4, with varying tire-road friction levels, are reported in Figs. 9(a)-(b), while the respective KPIs are in Table 3. For SMC, two configurations are considered, with the control input updated at: i) 1 ms, with the corresponding algorithm being referred to as 'SMC – 1 ms'; and ii) 10 ms, where the respective controller is referred to as 'SMC – 10 ms', which is aligned with the NMPC sampling time.

In the passive case, the traction capability is lost in the low-friction sections, leading to reduced vehicle speed. However, when the passive EV transitions from low-friction to high-friction conditions, e.g., at $s \approx 11$ m, it re-accelerates very promptly, because its wheels, already spinning at a higher speed than for the TCS cases, can grip the road surface very effectively. At the first high-to-low friction jump at $s \approx 6$ m, NMPC$^{(\text{w/o prev})}$ and NMPC$^{(\mu\ \text{prev})}$ show no difference along the ISO class B road test, with $\sigma_{peak} \approx 0.05$ in both cases. This is because the longitudinal slip threshold, see the "Reference" profile in the top subplot, is sufficiently high that the preview on μ alone does not enable the NMPC prediction model to pre-emptively foresee any longitudinal slip ratio constraint violation.

Thanks to its shorter time step, SMC – 1 ms better compensates the slip violations in the low-friction section than NMPC$^{(\mu\ \text{prev})}$, as shown for $s > 20$ m. As a consequence, SMC – 1 ms reduces $\hat{e}_\sigma$ by 51% and 40% for the ISO class B road, and by 52% and 49% for the ISO class C road, w.r.t. NMPC$^{(\text{w/o prev})}$ and NMPC$^{(\mu\ \text{prev})}$. However, SMC – 1 ms is not effective in the compensation of the slip ratio peaks following the high-to-low friction transitions. W.r.t.

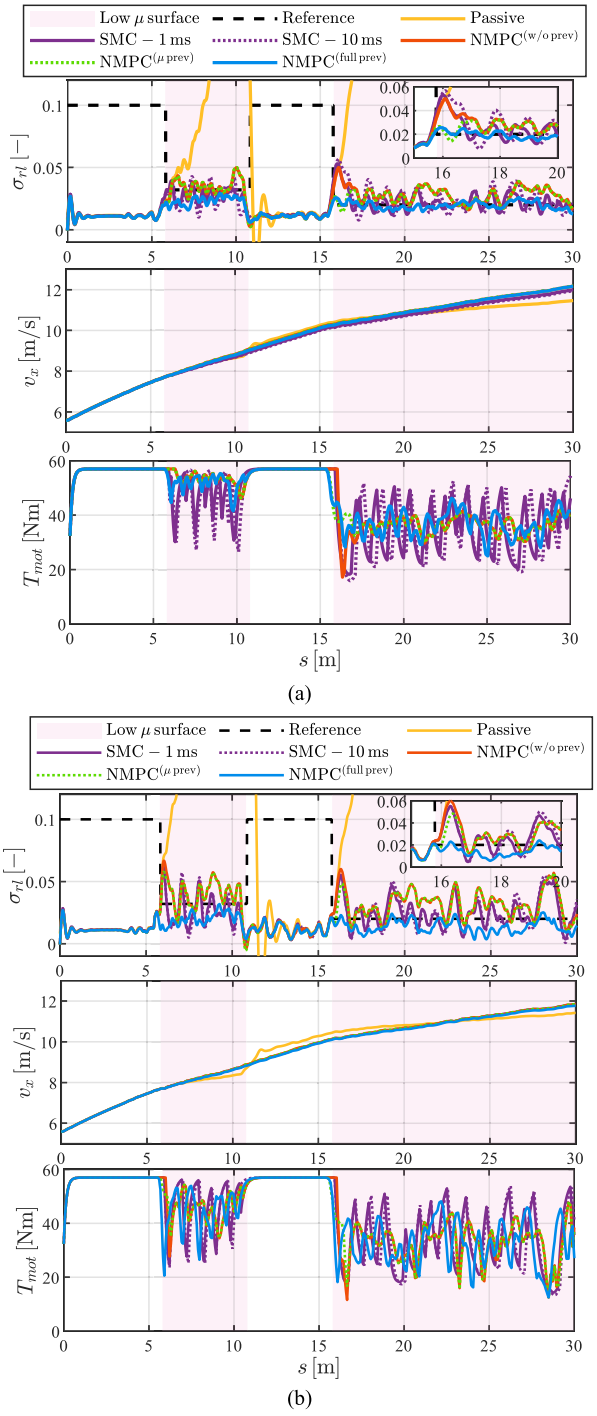

FIGURE 9. Performance comparison of the considered SMCs and NMPCs in terms of σ_{rl}, v_x, and T_{mot} profiles, along sections of (a) an ISO class B road and (b) an ISO class C road, with varying friction levels.

SMC – 1 ms, SMC – 10 ms is characterized by a general and evident performance degradation.

When the road profile information is included, which is the case of NMPC$^{(\text{full prev})}$, the controller can accurately anticipate the future variations in vertical tire load induced by the road irregularities, and intervenes in advance, as shown

by the T_{mot} profiles, to prevent any longitudinal tire slip threshold violation. In the most demanding conditions, such as the jump to the lowest μ level (0.3) at $s \approx 16$ m in Fig. 9(a), or throughout the operation over the more irregular class C profile in Fig. 9(b), NMPC$^{(\text{full prev})}$ delivers excellent performance with only marginal violations of the slip ratio constraint, and consistently ensures higher exit speed w.r.t. the passive EV. The KPIs in Table 2 confirm the superior wheel slip control capability of NMPC$^{(\text{full prev})}$, resulting into an approximately halved σ_{peak}, and an $\hat{e}_\sigma$ reduction by more than an order of magnitude w.r.t. SMC, NMPC$^{(\text{w/o prev})}$, and NMPC$^{(\mu\text{ prev})}$, particularly evident for the more demanding class C road.

TABLE 2. Controller KPIs for sections of an ISO class B road and an ISO class C road.

		σ_{peak} [-]	$\hat{e}_\sigma$ [-]	v_{fin} [m/s]
ISO class B road	SMC-1 ms	0.053	0.0021	11.40
	SMC-10 ms	0.061	0.0031	11.36
	NMPC$^{(\text{w/o prev})}$	0.050	0.0043	11.57
	NMPC$^{(\mu\text{ prev})}$	0.050	0.0035	11.58
	NMPC$^{(\text{full prev})}$	0.029	0.00037	11.56
ISO class C road	SMC-1 ms	0.062	0.0036	11.27
	SMC-10 ms	0.062	0.0040	11.26
	NMPC$^{(\text{w/o prev})}$	0.067	0.0076	11.25
	NMPC$^{(\mu\text{ prev})}$	0.057	0.0071	11.28
	NMPC$^{(\text{full prev})}$	0.032	0.00012	11.23

E. SPEED BUMP TESTS IN μ-SPLIT CONDITIONS

The scope is to evaluate the TCS performance for unbalanced friction conditions between the left and right tires, with the vehicle susceptible to lateral and yaw motions.

In the straight-line acceleration scenario in Fig. 10(a), the passive vehicle is characterized by significant lateral and yaw dynamics as the rear left wheel, excited by the bump, transitions onto the low-friction surface. This leads to an $|a_y|_{max}$ of 2.9 m/s^2, and requires substantial corrective steering action. SMC, NMPC$^{(\text{w/o prev})}$ and NMPC$^{(\mu\text{ prev})}$ only show marginal improvements in terms of reduced first peak of the longitudinal tire slip and decreased lateral acceleration oscillations. In contrast, thanks to its pre-emptive torque reduction, NMPC$^{(\text{full prev})}$ reduces σ_{peak} by 60% and 56% compared to NMPC$^{(\text{w/o prev})}$ and SMC. Additionally, the associated lateral dynamics remain negligible with minimal driver effort, corresponding to 82% and 66% $IACA_\delta$ reductions w.r.t. NMPC$^{(\text{w/o prev})}$ and NMPC$^{(\mu\text{ prev})}$.

The μ-split cornering test in Fig. 10(b) highlights how the NMPCs perform in a scenario with the additional mismatch caused by the absence of lateral dynamics in the prediction models. The transition of the rear left wheel onto the low-friction surface induces significant slip on the affected side, resulting in yaw rate deviations and curvature errors. SMC and NMPC$^{(\text{w/o prev})}$ provide partial mitigation of these effects, reducing $|a_y|_{max}$ to ~5 m/s^2 compared to the 5.6 m/s^2 of the passive configuration. Also in these conditions, NMPC$^{(\text{full prev})}$ has the most stable behavior,

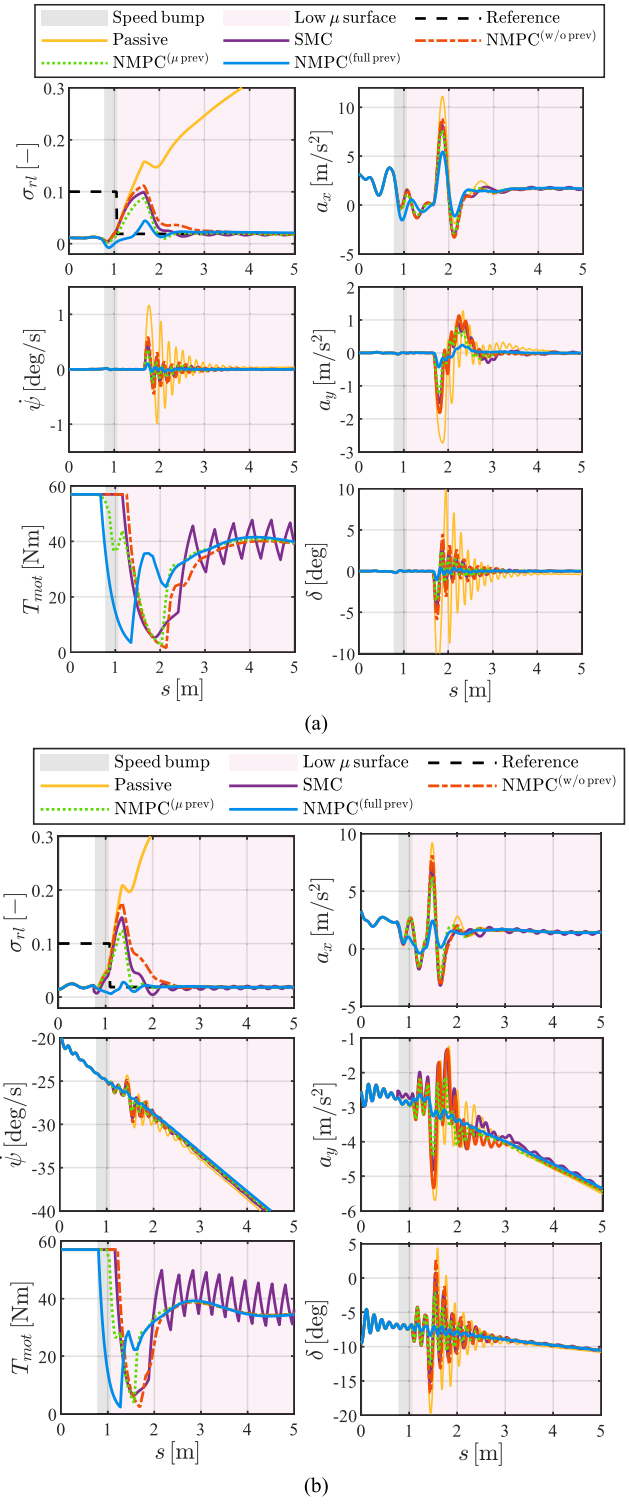

FIGURE 10. Performance comparison in terms of σ_{rl}, a_x, $\dot{\psi}$, a_y, a_x, T_{mot} and δ profiles as a function of s, for the considered speed bump test followed by a μ-split surface during: (a) straight-line conditions, starting from an initial speed of 30 km/h; and (b) quasi steady-state right-hand corner, starting from an initial speed of 10 km/h.

with negligible violations of the reference slip constraint, and minimal deviation from the expected longitudinal and lateral acceleration profiles. Such predictable behavior, also

in absence of the friction brake based actuation of the stability control function, highlights the potential of NMPC$^{(\text{full prev})}$ to enhance vehicle safety in challenging scenarios.

F. ROBUSTNESS ANALYSIS THROUGH MONTE CARLO SIMULATIONS

The target is to assess the controller robustness w.r.t. model uncertainties, disturbances, and mismatches between previewed and actual road profiles and tire–road friction levels, including both estimation errors in magnitude and time shifts (delays or advances) in the preview information.

The analysis is performed by means of Monte Carlo simulations that evaluate the performance of the considered SMC and NMPCs while varying some of the plant parameters during: (a) the speed bump test 1) described in Section IV-A; and (b) the straight-line speed bump μ-split test, referred to as test 3) in Section IV-A. The selected parameters, which are modified only in the high-fidelity plant model and remain fixed and equal to their nominal value in the prediction model, are:

- An additional mass, m_{add}, w.r.t. the nominal vehicle mass.
- A pure time delay, t_{del}, in the electric motor torque response, which was absent in the previous simulations with the nominal plant.
- A scaling factor, $\mu_{scal.}$, and a time shift, μ_{shift} (which can result either into an advance or a delay), applied to the tire-road friction factor.
- A scaling factor, $w_{scal.}$, and a time shift, w_{shift}, on the road profile.
- Scaling factors, w_{k_x} and w_{C_x}, on the longitudinal slip stiffness and longitudinal shape factor of the Pacejka tire model [43].

Since SMC does not include the vertical wheel dynamics within its formulation, it remains unaffected by errors in the effective road profile, i.e., $w_{scal.}$, and time shift, w_{shift}.

TABLE 3. Monte Carlo analysis results, in terms of average values and standard deviations of σ_{peak} and v_{fin}, as well as unfeasibility rate i_r, across the considered 500 simulations, for test 1) in Section IV-A.

	$\overline{\sigma_{peak}}$ [-]	$\overline{v_{fin}}$ [m/s]	σ^*_{peak} [-]	v^*_{fin} [m/s]	i_r [-]
SMC	0.152	7.88	0.025	0.201	-
NMPC$^{(\text{w/o prev})}$	0.156	7.83	0.032	0.245	0
NMPC$^{(\mu\text{ prev})}$	0.118	7.83	0.023	0.255	0
NMPC$^{(\text{full prev})}$	0.055	7.77	0.021	0.268	0

The Monte Carlo analysis covers 500 test scenarios for SMC and each NMPC configuration, defined by a combination of parameter values randomly drawn from the respective distributions in Fig. 11. Fig. 12(a) reports the resulting σ_{peak} and v_{fin} distributions for test (a), while Table 3 includes the respective average values, $\overline{\sigma_{peak}}$ and $\overline{v_{fin}}$, and standard deviations, σ^*_{peak} and v^*_{fin}. NMPC$^{(\text{full prev})}$ achieves nearly full compensation of the slip violations, corresponding to $\sigma_{peak} < 0.05$, for ∼60% of the considered cases, with a $\overline{\sigma_{peak}}$ of 0.055 and a σ^*_{peak} of 0.021, thus demonstrating minimal

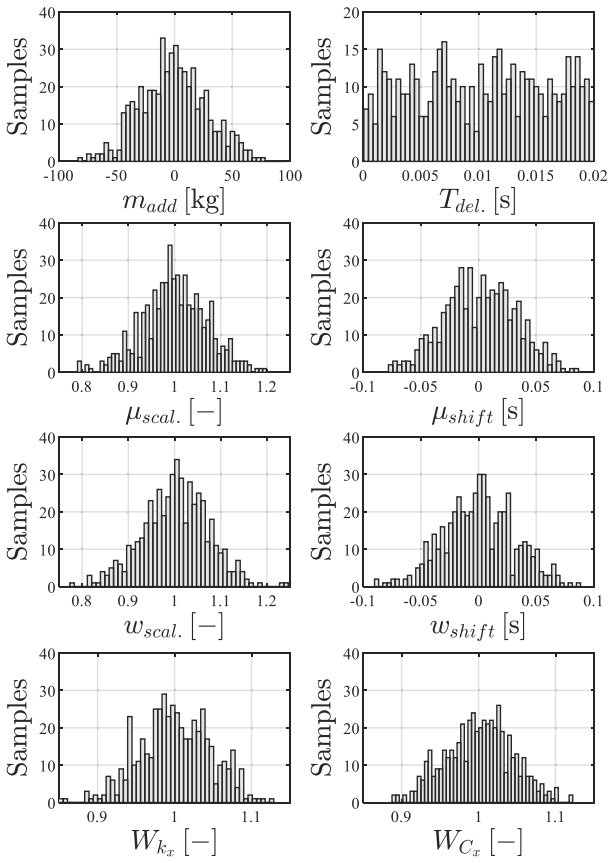

FIGURE 11. Implemented Monte Carlo parameters distributions.

performance degradation with parameter variations. On the contrary, NMPC$^{(\mu\text{ prev})}$, NMPC$^{(\text{w/o prev})}$ and the integral SMC exhibit significantly higher $\overline{\sigma_{peak}}$, amounting to 0.118, 0.156 and 0.152, with standard deviations σ^*_{peak} of 0.032, 0.023 and 0.025, leading to reduced traction performance and robustness. Even more, in presence of the worst-case friction and road-profile estimation errors, corresponding to scaling factors of ∼1.2 and preview time shifts of ∼0.1 s, for NMPC$^{(\text{full prev})}$ σ_{peak} remains below 0.13, whereas the μ-preview and no-preview NMPC configurations reach peak slip values of ∼0.16 and ∼0.19. This confirms that the full-preview formulation exhibits significantly contained degradation also under severe estimation inaccuracies. In parallel, the v_{fin} distribution reveals a negligible difference among the controller configurations, with a $\overline{v_{fin}}$ variation of less than 1%, i.e., the pre-emptive intervention of NMPC$^{(\text{full prev})}$ does not compromise the longitudinal vehicle dynamics.

Fig. 12(b) shows the distributions of σ_{peak}, $|a_y|_{max}$, and $IACA_\delta$ for the μ-split scenario, while Table 4 reports the average values and standard deviations of the selected KPIs. Similarly to the straight-line test case, NMPC$^{(\text{full prev})}$ reduces σ_{peak} by 42% w.r.t. NMPC$^{(\mu\text{ prev})}$, with similar values of the standard deviation among the configurations. Additionally, the inclusion of the road profile preview in NMPC$^{(\text{full prev})}$

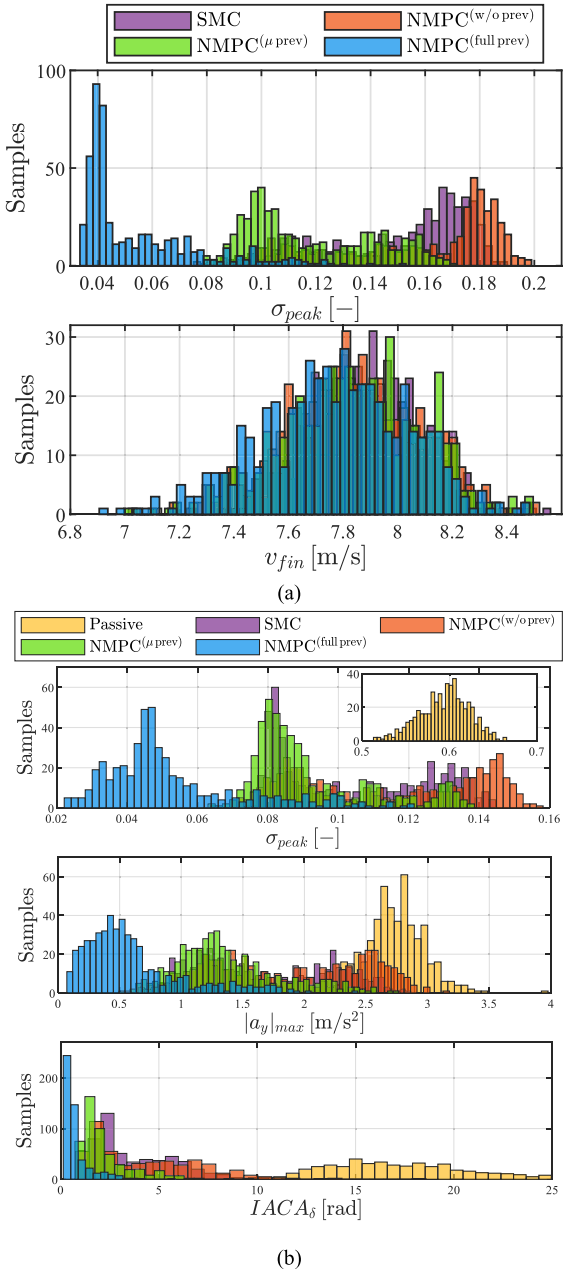

FIGURE 12. (a) σ_{peak} and v_{fin}; and (b) σ_{peak}, $|a_y|_{max}$ and $IACA_\delta$ distributions from the Monte Carlo analyses, respectively for the speed bump test 1) and the straight-line μ-split test in Section IV-A.

significantly attenuates $|a_y|_{max}$, whose average amounts to 0.60 m/s^2, and decreases the required steering corrections, with 65%, 82% and 80% reductions of the average values, and 47%, 75% and 65% reductions of the standard deviations, compared to NMPC$^{(\mu\ \text{prev})}$, NMPC$^{(\text{w/o prev})}$, and SMC. These results highlight the superior robustness of NMPC$^{(\text{full prev})}$ against disturbances and uncertainties, particularly in lateral dynamics conditions with asymmetric tire-road friction levels.

Finally, in Tables 3 and 4, i_r represents the unfeasibility rate, i.e., the number of samples for which the optimal control problem becomes unfeasible, or the associated numerical solver fails to find a solution. Its consistently zero value confirms the reliability and stability of the implemented NMPC algorithms in a broad range of conditions.

Although a formal stability proof cannot be provided for such a complex nonlinear control system, it was observed that, under free-response conditions, the cost function of the controller, integrated over the simulation time, tends to converge to zero. This behavior is consistent with Lyapunov stability theory, see the overview in [53] and its application to NMPC stability under simplifying assumptions in [54].

TABLE 4. Monte Carlo analysis results, in terms of average values and standard deviations of σ_{peak}, $|a_y|_{max}$ and $IACA_\delta$, as well as i_r, across the considered 500 simulations, for test 3) in Section IV-A.

	$\overline{\sigma_{peak}}$ [-]	$\overline{\lvert a_y\rvert_{max}}$ [m/s^2]	$\overline{IACA_\delta}$ [rad]	σ^*_{peak} [-]	$\lvert a_y\rvert^*_{max}$ [m/s]	$IACA^*_\delta$ [rad]	i_r [-]
SMC	0.105	1.68	3.89	0.022	0.547	1.95	-
NMPC$^{(\text{w/o prev})}$	0.114	1.87	4.27	0.026	0.614	2.77	0
NMPC$^{(\mu\ \text{prev})}$	0.092	1.38	2.24	0.017	0.429	1.30	0
NMPC$^{(\text{full prev})}$	0.053	0.60	0.77	0.020	0.408	0.68	0

VI. PROOF-OF-CONCEPT EXPERIMENTS

A. TESTING SET-UP

Preliminary proof-of-concept experiments were performed in the automated driving mode of the ZEBRA EV prototype introduced in Section II-B. While the simulations enabled broader sensitivity and robustness analyses, the experiments are a preliminary form of validation on the specific plant, operating with the typical uncertainties and disturbances of real-world conditions. In fact, if in the simulations the tire-road friction level is assumed to be known, in the experiments a constant nominal value is assumed for each surface section, leading to some unavoidable form of friction mismatch. Additional differences stem from the unmodeled dynamics and implementation effects, such as sensor noise, mechanical nonlinearities, and actuation and communication latencies (e.g., those associated with the power electronics, CAN bus, and real-time control hardware).

Fig. 13 illustrates the vehicle testing set-up, which mirrors the simulated speed bump test scenario, involving an obstacle followed by a low-friction surface implemented through soap on acrylic boards, which corresponds to $\mu \approx 0.2$.

To run the NMPCs in real-time on the available dSPACE MicroAutoBox II unit and deal with the particularly slow transient response of the ZEBRA powertrain, see Fig. 3, differently from the simulation phase in Section V, during the experiments the NMPC settings were adjusted through a variable time step strategy along H_p [55]. Specifically, H_p is set to 240 ms, consisting of 4 initial short time steps of 10 ms each, followed by 4 longer steps of 50 ms each, while maintaining a controller implementation time of 10 ms. The integration step of the prediction model was increased from 1 to 5 ms. The measured turnaround time of the dSPACE unit during the experimental tests remains well below the sampling time, with a maximum value of ∼7.7 ms and an

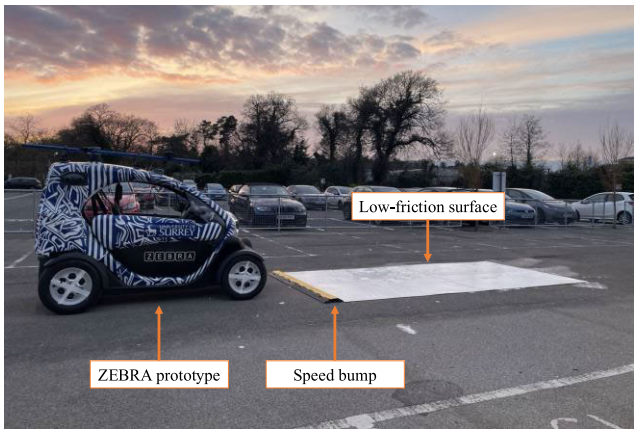

FIGURE 13. The ZEBRA EV of the University of Surrey along the test scenario involving a speed bump followed by a low-μ section obtained through soap on acrylic boards.

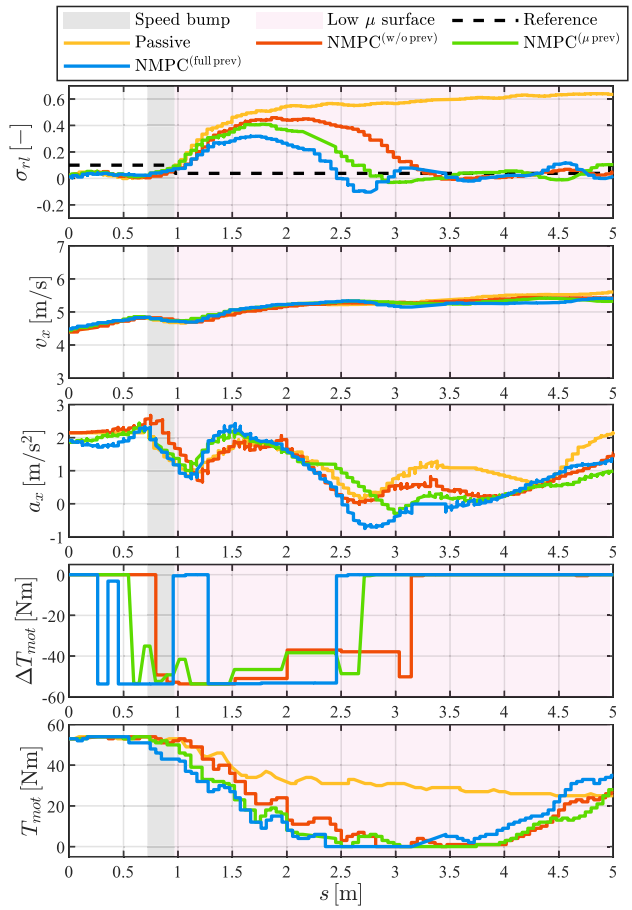

FIGURE 14. Performance comparison of the considered NMPCs in terms of σ_{rl}, v_x, a_x, ΔT_{mot}, and T_{mot} profiles, along the experimental speed bump test.

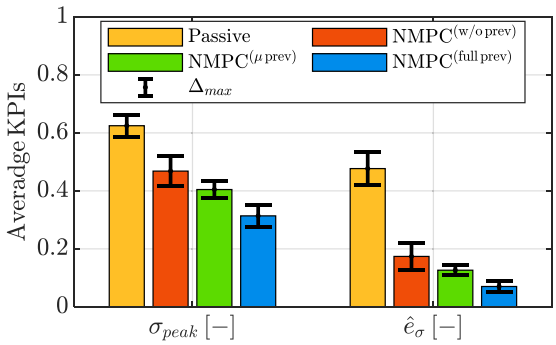

FIGURE 15. σ_{peak} and $\hat{e}_\sigma$ for the rear left corner, across the 24 experimental speed bump tests covering the considered NMPC configurations, where the histograms refer to the average values and the error bars to the range of the respective KPI.

average value of ∼7.2 ms. Moreover, in the experiments, because of the significant pure time delay in the powertrain torque response, which was absent in the simulations and is visible in Fig. 3, the preview information – provided to NMPC$^{(full\ prev)}$ and NMPC$^{(\mu\ prev)}$ as online data – is shifted by an interval corresponding to the pure time delay, which originates a lead component in the signal flow to the NMPC algorithm. In the vehicle tests, the same lead shift was applied also to the tire-road friction factor information provided to NMPC$^{(w/o\ prev)}$, which – otherwise, given the extent of the pure time delay and slow powertrain dynamics – would have originated a slip ratio response close to the one of the passive EV. Hence, in comparison with the corresponding simulated configuration in Section V, the experimental NMPC$^{(w/o\ prev)}$ set-up includes an intrinsic form of tire-road friction preview, although the μ information remains constant along H_p, while no road elevation data is provided to the algorithm.

B. EXPERIMENTAL RESULTS

To verify the consistency of the results, for each considered controller configuration, the same experimental maneuver was repeated six times. Fig. 14 reports the profiles of the main variables as a function of s, along one of the experimental runs for each controller, while the histograms of Fig. 15 plot the average values of the longitudinal slip KPIs across the test repetitions, together with the corresponding ranges of σ_{peak} and $\hat{e}_\sigma$. Interestingly, due to the very slow response of the specific powertrain, the NMPCs exhibit a "bang-bang" behavior, with abrupt reference motor torque variations, see the resulting ΔT_{mot} profiles. Due to the actuation delay compensation strategy discussed in Section VI-A, in the experiments also NMPC$^{(w/o\ prev)}$ intervenes before the μ-jump. The pre-emptive intervention of NMPC$^{(full\ prev)}$, corresponding to the initial drastic ΔT_{mot} request before the obstacle is reached, effectively decreases the violation of the soft constraint on the tire slip, thanks to the consideration of the vertical dynamics caused by the road irregularity, which is not the case for NMPC$^{(\mu\ prev)}$ and NMPC$^{(w/o\ prev)}$. In fact, while NMPC$^{(full\ prev)}$ manages to limit σ_{peak} down to 0.31, both NMPC$^{(\mu\ prev)}$ and NMPC$^{(w/o\ prev)}$ are characterized by σ_{peak} values in excess of 0.4, leading to ∼23% reduction. Negligible differences are observed in terms of vehicle speed and longitudinal acceleration. In the second half of the test, the magnitude of the control action decreases, see ΔT_{mot} at

$\sim$2.5 m for NMPC$^{(\text{full prev})}$. This occurs since the controllers are informed of the upcoming high-friction conditions at the exit of the acrylic boards. Because of the slow response, the feedback motor torque T_{mot}, estimated by the inverter, lags due to the powertrain delay and slow actuator response. The KPIs confirm the significant improvement provided by NMPC$^{(\text{full prev})}$, e.g., capable of nearly halving $\hat{e}_\sigma$ w.r.t. the benchmarking state-of-the-art NMPC$^{(\mu\ \text{prev})}$ implementation. Such preliminary experimental results are repeatable and consistent, as shown by the narrow error bars, for example highlighting a maximum σ_{peak} variation amounting to $\sim$6% w.r.t. its average value for NMPC$^{(\text{full prev})}$, and proportional variations of the indicators for the other considered controller configurations.

VII. CONCLUSION

The study introduced a novel nonlinear model predictive control (NMPC) formulation for traction control in electric vehicles with centralized on-board powertrains, preemptively considering the vertical dynamics effects caused by road irregularities. The simulation results highlight that:

- For the nominal powertrain with a torque time constant τ of 25 ms, the combination of a prediction horizon $H_p = 90$ ms and controller sampling time $T_s = 10$ ms strikes a good balance between tire slip control on irregular roads and computational load.
- For localized road events, the NMPC formulation with preview on both the tire-road friction level and road profile, i.e., NMPC$^{(\text{full prev})}$, can achieve nearly complete compensation of the violations of the longitudinal tire slip constraint, together with a higher exit speed of the vehicle w.r.t. the passive case.
- When considering slower powertrain response characteristics than those of the nominal vehicle, the benefit of NMPC$^{(\text{full prev})}$ on the considered localized road event further increases, with $>$2.5 and $>$7 times reductions of the time integrals of the tire slip violations, for $\tau = 120$ ms, w.r.t. NMPC$^{(\mu\ \text{prev})}$, including preview only on the tire-road friction level, and the TCSs without any form of road preview, i.e., NMPC$^{(\text{w/o prev})}$ and SMC.
- NMPC$^{(\text{full prev})}$ is more robust than NMPC$^{(\mu\ \text{prev})}$ and NMPC$^{(\text{w/o prev})}$ against model uncertainties, disturbances, and inaccuracies in the road profile and friction coefficient estimation, which was shown through a Monte Carlo analysis, covering also μ-split conditions.
- The promising NMPC$^{(\text{full prev})}$ results are confirmed over sections of ISO class B and class C roads.

The preliminary proof-of-concept speed bump test experiments confirm the simulation results with good repeatability. The potential safety performance improvements highlighted by this study suggest that the proposed preview-based formulation could be transformative for the next TCS generations. Future developments will include: i) extensive validation of the proposed controller through experiments covering a broad range of conditions, including μ-split and cornering scenarios; ii) the integration of real-time preview-capable tire-road friction estimation and road irregularity detection algorithms based on exteroceptive on-board sensing and V2X; iii) the integration of additional functionalities within the same NMPC formulation, such as continuous longitudinal and vertical comfort control as well as vehicle stability control through friction brake actuation; and iv) the development of learning-based control strategies, such as imitation learning, to reproduce the NMPC behavior while reducing the computational load.

REFERENCES

[1] D. Yang, K. Jiang, D. Zhao, C. Yu, Z. Cao, S. Xie, Z. Xiao, X. Jiao, S. Wang, and K. Zhang, "Intelligent and connected vehicles: Current status and future perspectives," *Sci. China Technological Sci.*, vol. 61, no. 10, pp. 1446–1471, Oct. 2018.

[2] H. Zhou, W. Xu, J. Chen, and W. Wang, "Evolutionary V2X technologies toward the Internet of Vehicles: Challenges and opportunities," *Proc. IEEE*, vol. 108, no. 2, pp. 308–323, Feb. 2020.

[3] M. Noor-A-Rahim, Z. Liu, H. Lee, M. O. Khyam, J. He, D. Pesch, K. Moessner, W. Saad, and H. V. Poor, "6G for vehicle-to-everything (V2X) communications: Enabling technologies, challenges, and opportunities," *Proc. IEEE*, vol. 110, no. 6, pp. 712–734, Jun. 2022.

[4] Volvo. (2014). *Volvo Cars Puts 1000 Test Cars to Use: Scandinavian Cloud-Based Project for Sharing Road-Condition Information Becomes a Reality*. [Online]. Available: https://www.media.volvocars.com.

[5] U. Montanaro, S. Dixit, S. Fallah, M. Dianati, A. Stevens, D. Oxtoby, and A. Mouzakitis, "Towards connected autonomous driving: Review of use-cases," *Vehicle Syst. Dyn.*, vol. 57, no. 6, pp. 779–814, Jun. 2019.

[6] C. Göhrle, A. Schindler, A. Wagner, and O. Sawodny, "Road profile estimation and preview control for low-bandwidth active suspension systems," *IEEE/ASME Trans. Mechatronics*, vol. 20, no. 5, pp. 2299–2310, Oct. 2015.

[7] J. Theunissen, A. Sorniotti, P. Gruber, S. Fallah, M. Ricco, M. Kvasnica, and M. Dhaens, "Regionless explicit model predictive control of active suspension systems with preview," *IEEE Trans. Ind. Electron.*, vol. 67, no. 6, pp. 4877–4888, Jun. 2020.

[8] J. Wu, H. Zhou, Z. Liu, and M. Gu, "Ride comfort optimization via speed planning and preview semi-active suspension control for autonomous vehicles on uneven roads," *IEEE Trans. Veh. Technol.*, vol. 69, no. 8, pp. 8343–8355, Aug. 2020.

[9] B.-S. Kwon, D. Kang, and K. Yi, "Wheelbase preview control of an active suspension with a disturbance-decoupled observer to improve vehicle ride comfort," *Proc. Inst. Mech. Eng., D, J. Automobile Eng.*, vol. 234, no. 6, pp. 1725–1745, May 2020.

[10] A. Alshawi, S. De Pinto, P. Stano, S. van Aalst, K. Praet, E. Boulay, D. Ivone, P. Gruber, and A. Sorniotti, "An adaptive unscented Kalman filter for the estimation of the vehicle velocity components, slip angles, and slip ratios in extreme driving manoeuvres," *Sensors*, vol. 24, no. 2, p. 436, Jan. 2024.

[11] S. Khaleghian, A. Emami, and S. Taheri, "A technical survey on tire-road friction estimation," *Friction*, vol. 5, no. 2, pp. 123–146, Jun. 2017.

[12] W. Cai, X. Wu, M. Zhou, Y. Liang, and Y. Wang, "Review and development of electric motor systems and electric powertrains for new energy vehicles," *Automot. Innov.*, vol. 4, no. 1, pp. 3–22, Feb. 2021.

[13] M. Jalali, A. Khajepour, S.-K. Chen, and B. Litkouhi, "Integrated stability and traction control for electric vehicles using model predictive control," *Control Eng. Pract.*, vol. 54, pp. 256–266, Sep. 2016.

[14] A. Scamarcio, P. Gruber, S. De Pinto, and A. Sorniotti, "Anti-jerk controllers for automotive applications: A review," *Annu. Rev. Control*, vol. 50, pp. 174–189, Jan. 2020.

[15] L. M. Castellanos Molina, R. Manca, S. Hegde, N. Amati, and A. Tonoli, "Predictive handling limits monitoring and agility improvement with torque vectoring on a rear in-wheel drive electric vehicle," *Vehicle Syst. Dyn.*, vol. 62, no. 9, pp. 1–25, Sep. 2024.

[16] N. Guo, J. Liu, J. Li, W. Chen, Y. Zhang, Q. Lu, and Z. Chen, "Handling-stability control for distributed drive electric vehicles via Lyapunov-based nonlinear MPC algorithm," *IEEE Trans. Transport. Electrific.*, vol. 11, no. 2, pp. 6615–6628, Apr. 2025.

[17] S. Kopylov, G. Phanomchoeng, M. Ambrož, Ž. Petan, R. Kunc, and Y. Qiu, "Improvements to a vehicle's ride comfort by controlling the vertical component of the driving force based on in-wheel motors," *J. Vibrat. Control*, vol. 29, nos. 17–18, pp. 4001–4014, Sep. 2023.

[18] Y. Li, D. Ma, Z. An, Z. Wang, Y. Zhong, S. Chen, and C. Feng, "V2X-sim: Multi-agent collaborative perception dataset and benchmark for autonomous driving," *IEEE Robot. Autom. Lett.*, vol. 7, no. 4, pp. 10914–10921, Oct. 2022.

[19] L. Zhao, H. Chai, Y. Han, K. Yu, and S. Mumtaz, "A collaborative V2X data correction method for road safety," *IEEE Trans. Rel.*, vol. 71, no. 2, pp. 951–962, Jun. 2022.

[20] A. Musa, M. Pipicelli, M. Spano, F. Tufano, F. De Nola, G. Di Blasio, A. Gimelli, D. A. Misul, and G. Toscano, "A review of model predictive controls applied to advanced driver-assistance systems," *Energies*, vol. 14, no. 23, p. 7974, Nov. 2021.

[21] S. Tao, Y. Liu, S. Zhou, and H. Wei, "Integrated path following and adaptive front-light control of autonomous vehicles: A unified MPC approach," in *Proc. IEEE 3rd Ind. Electron. Soc. Annu. On-Line Conf. (ONCON)*, Beijing, China, Dec. 2024.

[22] P. Stano, U. Montanaro, D. Tavernini, M. Tufo, G. Fiengo, L. Novella, and A. Sorniotti, "Model predictive path tracking control for automated road vehicles: A review," *Annu. Rev. Control*, vol. 55, pp. 194–236, Jan. 2023.

[23] Y. Sun, P. Wang, and F. Liu, "Design and implementation of cooperative adaptive cruise control based on V2X," in *IEEE MTT-S Int. Microw. Symp. Dig.*, Shanghai, China, Sep. 2020, pp. 1–3.

[24] J. Li, C. Chen, F. Gao, B. Yang, and X. Guan, "V2X based cooperative motion control and energy management for electronic vehicles," in *Proc. IEEE 98th Veh. Technol. Conf. (VTC-Fall)*, Hong Kong, Hong Kong, Oct. 2023, pp. 1–5.

[25] A. L. Gratzer, M. M. Broger, A. Schirrer, and S. Jakubek, "Two-layer MPC architecture for efficient mixed-integer-informed obstacle avoidance in real-time," *IEEE Trans. Intell. Transp. Syst.*, vol. 25, no. 10, pp. 13767–13784, Oct. 2024.

[26] K. M. So, G. Tavolo, D. Tavernini, M. Grosso, S. Pozzato, P. Perlo, and A. Sorniotti, "Novel pre-emptive control solutions for V2X connected electric vehicles," in *Proc. Transp. Res. Arena (TRA) Conf.*, Lisbon, Portugal, 2022, pp. 1–8.

[27] V. Vidal, P. Stano, G. Tavolo, M. Dhaens, D. Tavernini, P. Gruber, and A. Sorniotti, "On pre-emptive in-wheel motor control for reducing the longitudinal acceleration oscillations caused by road irregularities," *IEEE Trans. Veh. Technol.*, vol. 71, no. 9, pp. 9322–9337, Sep. 2022.

[28] P. Stano, D. Lazzarini, S. Santoro, M. Mihalkov, U. Montanaro, A. Vigliani, A. Ferrara, M. Dhaens, and A. Sorniotti, "On-board electric powertrain control for the compensation of the longitudinal acceleration oscillations caused by road irregularities," *Mechanism Mach. Theory*, vol. 202, Nov. 2024, Art. no. 105759.

[29] A. Scamarcio, C. Caponio, M. Mihalkov, P. Georgiev, J. Ahmadi, K. M. So, D. Tavernini, and A. Sorniotti, "Predictive anti-jerk and traction control for V2X connected electric vehicles with central motor and open differential," *IEEE Trans. Veh. Technol.*, vol. 72, no. 6, pp. 7221–7239, Jun. 2023.

[30] G. Tavolo, K. M. So, D. Tavernini, P. Perlo, and A. Sorniotti, "Nonlinear model predictive control for preview-based traction control," in *Proc. 15th Int. Symp. Adv. Vehicle Control*, Kanagawa, Japan, 2022, pp. 1–6.

[31] G. Tavolo, K. M. So, D. Tavernini, P. Perlo, and A. Sorniotti, "On antilock braking systems with road preview through nonlinear model predictive control," *IEEE Trans. Ind. Electron.*, vol. 71, no. 8, pp. 9436–9448, Aug. 2024.

[32] Ford Global Technologies, "Traction control system and method," U.S. Patent 20060293841A1, Dec. 28, 2006.

[33] L. Q. Mou, X. Q. Lin, S. M. He, Y. Y. He, B. W. Zhao, X. Z. Song, J. S. You, and F. F. Huang, "Predictive traction control system of vehicle based on road surface information and predictive traction control method," U.S. Patent 2023125472A1, Jul. 6, 2023.

[34] L. Birch, D. Lausecker, J. Kelly, and S. A. Ali, "Traction determination by changing wheel normal force," U.S. Patent 20240001932A1, Jan. 4, 2024.

[35] A. Mistry, D. Lausecker, S. Brown, S. A. Ali, L. Birch, W. Burdock, and J. Kelly, "Traction-dependent variation of wheel-to-surface normal force," U.S. Patent 20240109385A1, Apr. 4, 2024.

[36] J. Adcox, B. Ayalew, T. Rhyne, S. Cron, and M. Knauff, "Interaction of anti-lock braking systems with tire torsional dynamics," *Tire Sci. Technol.*, vol. 40, no. 3, pp. 171–185, Oct. 2012.

[37] H. A. Hamersma and P. Schalk Els, "Improving the braking performance of a vehicle with ABS and a semi-active suspension system on a rough road," *J. Terramechanics*, vol. 56, pp. 91–101, Dec. 2014.

[38] S. Aghasizade, M. Mirzaei, and S. Rafatnia, "The effect of road quality on integrated control of active suspension and anti-lock braking systems," *AUT J. Mech. Eng.*, vol. 3, no. 1, pp. 123–135, 2019.

[39] S. Biju, A. Chammam, S. Askar, P. Rodrigues, and M. Jalalnezhad, "Prediction-based controller radial neural network for the traction control system," *J. Vibrat. Control*, vol. 32, nos. 5–6, pp. 898–912, Mar. 2026.

[40] C. Caponio, M. Mihalkov, Z. Hankovszki, H. Fuse, H., V. Ivanov, A. Sorniotti, P. Gruber, and U. Montanaro, "Development of deep reinforcement learning traction controllers for front and rear wheel drive electrified vehicles," SAE Tech. Paper 2025-01-8803, 2025.

[41] S. De Pinto, P. Camocardi, C. Chatzikomis, A. Sorniotti, F. Bottiglione, G. Mantriota, and P. Perlo, "On the comparison of 2- and 4-wheel-drive electric vehicle layouts with central motors and single- and 2-speed transmission systems," *Energies*, vol. 13, no. 13, p. 3328, Jun. 2020.

[42] *Siemens Digital Industries Software*, Simcenter Tyre-MF-Tyre/MF-Swift User Manual, Plano, TX, USA, 2020.

[43] H. B. Pacejka, *Tire and Vehicle Dynamics*, 3rd ed. Oxford, U.K.: Butterworth-Heinemann, 2012.

[44] A. J. C. Schmeitz and W. D. Versteden, "Structure and parameterization of MF-swift, a magic formula-based rigid ring tire Model3," *Tire Sci. Technol.*, vol. 37, no. 3, pp. 142–164, Sep. 2009.

[45] A. J. C. Schmeitz, "A semi-empirical three-dimensional model of the pneumatic tyre rolling over arbitrarily uneven road surfaces," Ph.D. thesis, Dept. Mech. Eng., Delft Univ. Technol., Delft, The Netherlands, 2004.

[46] R. Quirynen, M. Vukov, M. Zanon, and M. Diehl, "Autogenerating microsecond solvers for nonlinear MPC: A tutorial using ACADO integrators," *Optim. Control Appl. Methods*, vol. 36, no. 5, pp. 685–704, Sep. 2015.

[47] *Mechanical Vibration, Road Surface Profiles*, Standard ISO 8608:2016, 2016.

[48] P. Múčka, "Simulated road profiles according to ISO 8608 in vibration analysis," *J. Test. Eval.*, vol. 46, no. 1, pp. 405–418, Jan. 2018.

[49] D. Savitski, V. Ivanov, K. Augsburg, T. Emmei, H. Fuse, H. Fujimoto, and L. M. Fridman, "Wheel slip control for the electric vehicle with in-wheel motors: Variable structure and sliding mode methods," *IEEE Trans. Ind. Electron.*, vol. 67, no. 10, pp. 8535–8544, Oct. 2020.

[50] D. Savitski, D. Schleinin, V. Ivanov, and K. Augsburg, "Robust continuous wheel slip control with reference adaptation: Application to the brake system with decoupled architecture," *IEEE Trans. Ind. Informat.*, vol. 14, no. 9, pp. 4212–4223, Sep. 2018.

[51] D. Tavernini, M. Metzler, P. Gruber, and A. Sorniotti, "Explicit nonlinear model predictive control for electric vehicle traction control," *IEEE Trans. Control Syst. Technol.*, vol. 27, no. 4, pp. 1438–1451, Jul. 2019.

[52] *Mechanical Vibration and Shock-Evaluation of Human Exposure to Whole-Body Vibration-Part 1: General Requirements*, Standard ISO 2631-1:1997, 1997.

[53] N. Bof, R. Carli, and L. Schenato, "Lyapunov theory for discrete time systems," 2018, *arXiv:1809.05289*.

[54] A. Grancharova and T. A. Johansen, *Explicit Nonlinear Model Predictive Control*. Cham, Switzerland: Springer, 2012.

[55] S. Erlien, S. Fujita, and J. C. Gerdes, "Safe driving envelopes for shared control of ground vehicles," *Adv. Automot. Control*, vol. 46, no. 21, pp. 831–836, 2013.

RAFFAELE MANCA received the M.Sc. degree in automotive engineering from Politecnico di Torino, Turin, Italy, in 2020, where he is currently pursuing the Ph.D. degree in mechanical engineering. His research interests include the electrification of powertrain and chassis components, and vehicle dynamics modeling and control.

PIETRO STANO received the M.Sc. degree in mechanical engineering from Politecnico di Torino, Turin, Italy, in 2020, and the Ph.D. degree in automotive engineering from the University of Surrey, Guildford, U.K., in 2024. His research interests include vehicle dynamics modeling and control applied to electric and automated vehicles.

MARIO MIHALKOV received the M.Sc. degree in electrical engineering from Aalborg University, Aalborg, Denmark, in 2018. He is currently pursuing the Ph.D. degree in advanced vehicle engineering with the University of Surrey, Guildford, U.K. His current research interests include advanced model-based and machine learning algorithms for vehicle dynamics control.

LUIS M. CASTELLANOS MOLINA received the M.Sc. degree in energy efficiency from Cienfuegos University, Cuba, and the Ph.D. degree in mechanical engineering from Politecnico di Torino, Italy, in 2020. He was a Research Assistant and a Junior Lecturer with Cienfuegos University, from 2013 to 2015. He is currently a Postdoctoral Researcher with Politecnico di Torino. His research interests include model predictive control and its applications to magnetic suspension systems.

UMBERTO MONTANARO received the M.Sc. degree in computer science engineering, the Ph.D. degree in control engineering, and the Ph.D. degree in mechanical engineering from the University of Naples Federico II, Naples, Italy, in 2005, 2009, and 2016, respectively. He is currently a Senior Lecturer of control engineering and autonomous systems with the University of Surrey, Guildford, U.K. His research interests include adaptive control, and control of piecewise-affine, mechatronic, and automotive systems.

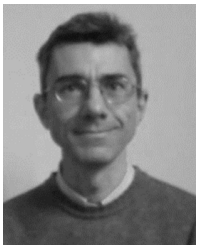

ANDREA TONOLI received the Ph.D. degree, in 1993. He is currently a Full Professor with the Mechanical and Aerospace Engineering Department, Politecnico di Torino. He is the Founder of the Mechatronics Laboratory, the Coordinator of the Automotive Engineering M.Sc. and B.Sc. Programs, and the Coordinator of Spoke 2 (Sustainable Road Vehicle) at the National Sustainable Mobility Center (MOST). His research interests include vehicle electrification in chassis and powertrain systems, active, passive, and regenerative shock absorbers, powertrain hybridization, and energy management.

ALDO SORNIOTTI (Member, IEEE) received the M.Sc. degree in mechanical engineering and the Ph.D. degree in applied mechanics from Politecnico di Torino, Turin, Italy, in 2001 and 2005, respectively. He is currently a Full Professor of applied mechanics with Politecnico di Torino, after being a Professor and the Head of the Centre of Automotive Engineering, University of Surrey, Guildford, U.K. His research interests include vehicle dynamics control for electric and automated vehicles.